

RESEARCH ARTICLE

10.1029/2019JB018363

Key Points:

- Experiments on a 3-m rock show nucleation at many locations, including at the edges of creeping regions, consistent with numerical models
- Loading perturbations and mild strength heterogeneity produce order of magnitude variations in estimates of nucleation length scale
- Earthquake initiation on heterogeneous faults is better characterized by critical power density than a time-invariant critical length scale

Correspondence to:

G. C. McLaskey,
gcm8@cornell.edu

Citation:

McLaskey, G. C. (2019). Earthquake Initiation From Laboratory Observations and Implications for Foreshocks. *Journal of Geophysical Research: Solid Earth*, 124, 12,882–12,904. <https://doi.org/10.1029/2019JB018363>

Received 11 JUL 2019

Accepted 5 NOV 2019

Accepted article online 11 NOV 2019

Published online 4 DEC 2019

Earthquake Initiation From Laboratory Observations and Implications for Foreshocks

Gregory C. McLaskey¹ 

¹School of Civil and Environmental Engineering, Cornell University, Ithaca, NY, USA

Abstract This paper reviews laboratory observations of earthquake initiation and describes new experiments on a 3-m rock sample where the nucleation process is imaged in detail. Many of the laboratory observations are consistent with previous work that showed a slow and smoothly accelerating earthquake nucleation process that expands to a critical nucleation length scale L_c , before it rapidly accelerates to dynamic fault rupture. The experiments also highlight complexities not currently considered by most theoretical and numerical models. This includes a loading rate dependency where a “kick” above steady state produces smaller and more abrupt initiation. Heterogeneity of fault strength also causes abrupt initiation when creep fronts coalesce on a stuck patch that is somewhat stronger than the surrounding fault. Taken together, these two mechanisms suggest a rate-dependent “cascade up” model for earthquake initiation. This model simultaneously accounts for foreshocks that are a by-product of a larger nucleation process and similarities between initial P wave signatures of small and large earthquakes. A diversity of nucleation conditions are expected in the Earth’s crust, ranging from slip limited environments with $L_c < 1$ m, to ignition-limited environments with $L_c > 10$ km. In the latter case, L_c fails to fully characterize the initiation process since earthquakes nucleate not because a slipping patch reaches a critical length but because fault slip rate exceeds a critical power density needed to ignite dynamic rupture.

Plain Language Summary In uniquely large-scale laboratory experiments, a 3-m rock sample is squeezed until earthquake-like slip events spontaneously develop on a planar fault cut through the sample. This paper describes the initiation of those slip events—where one part of the fault begins to slip a fraction of a second before the rest of it ruptures (i.e., preslip). The laboratory observations are compared to theoretical models, computer simulations, and field studies of foreshock sequences and other earthquake precursors. Many observations are consistent with previous work that showed slow and smoothly accelerating earthquake initiation—a process termed earthquake nucleation. When the preslip region grows larger than a critical length scale L_c (~1 m), it accelerates unstably and radiates seismic waves like an earthquake. However, some observations show an order of magnitude variation in apparent L_c . The initiation process is sensitive to details such as naturally occurring variation in the strength of the rock/rock fault and perturbations in the rate at which the rock is loaded. Put together, the laboratory work suggests that smoothly accelerating earthquake nucleation is a property of unnaturally smooth and homogenous faults and that L_c is an incomplete metric for characterizing the initiation of earthquakes on realistically rough natural faults.

1. Introduction

The enigmatic earthquake initiation process is fleeting, mercurial, and challenging both to characterize and observe. Yet it is intimately related to problems of earthquake production, prediction, and rapid magnitude estimation and is therefore hugely important for earthquake science. Laboratory observations and theoretical arguments indicate that earthquakes start slowly and must grow and accelerate before they radiate seismic waves. This beginning, illustrated schematically in Figure 1, is at first quasistatic and aseismic and is referred to as earthquake nucleation. A localized region known as the nucleation zone first starts to slip. Shear stress drops within the nucleation zone and intensifies near the edges that are the tips of a quasistatic shear crack. Stresses concentrated near the crack tip can promote slow expansion of the nucleation zone (crack growth). During this slow beginning, rupture expansion velocity $V_r < 0.01V_s$, where V_s is the shear wave velocity. At time t_{in} , the shear crack reaches a critical state, typically characterized by crack length L_c . At this point, V_r rapidly accelerates to a significant fraction of V_s , and slip rate rapidly approaches 1 m/s. Seismic waves are radiated, and an earthquake is born.

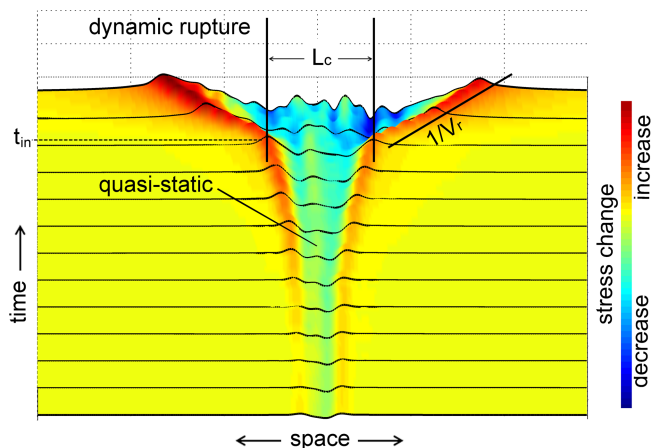


Figure 1. Schematic description of the initiation of dynamic rupture according to a smooth nucleation model. Slow, localized slip near the center of the region grows to a critical length L_c before accelerating to seismic slip speeds and rupture velocity V_r . The black horizontal lines and colors denote local shear stress changes that result from the slip. Adapted from Ohnaka (2000).

Detecting earthquake nucleation is a challenge. In laboratory experiments on rocks, nucleation-related slow slip is most easily detected with arrays of strain gages, and a 0.01- to 1-m-sized nucleation zone is sometimes observed in milliseconds before a stick-slip instability. Often this nucleation process is characterized with distinct phases (Johnson & Scholz, 1976; McLaskey & Kilgore, 2013; Ohnaka & Kuwahara, 1990; Ohnaka & Shen, 1999; Okubo & Dieterich, 1984). Borehole strain meters in the Earth have thus far not detected any similar nucleation processes (Roeloffs, 2006), despite efforts at Parkfield, CA (Johnston et al., 2006).

Theoretical and numerical studies of earthquake initiation have explored the characteristics of nucleation, based on either linear slip weakening friction (Andrews, 1976; Campillo & Ionescu, 1997; Uenishi & Rice, 2003), or rate- and state-dependent friction (Ampuero & Rubin, 2008; Dieterich, 1992; Fang et al., 2010; Rubin & Ampuero, 2005, 2009; Viesca, 2016). One common outcome of these studies is the determination of the critical nucleation length-scale L_c (often termed h^*) and its dependence on elastic and friction parameters, as discussed in section 2.2.

This study aims to describe earthquake initiation observations from laboratory experiments and compare previous work to new observations

of rupture initiation from a 3-m machine at Cornell University. The laboratory results are then compared with theoretical and numerical models and extended to the stress levels and length scales of the seismogenic crust. Ultimately, it is hoped that our understanding of nucleation can be used to categorize and inform our expectations for natural faults and larger earthquakes. Of particular interest is the interpretation of foreshocks based on cascade- or preslip-type earthquake initiation models (Beroza & Ellsworth, 1996).

This work focuses on the mechanical aspects of the earthquake initiation process, obtained primarily from local fault slip measurements. Laboratory observations of seismic indicators such as foreshocks and tremors (McLaskey & Kilgore, 2013; Zhuo et al., 2018) will be the focus of a future study, though seismic implications of various nucleation models are considered in section 6. Earthquake nucleation is intimately related to stability, so this study may also have relevance to our understanding of slow earthquakes, which might be considered unsuccessful earthquake nucleation attempts (e.g., Liu & Rice, 2005).

The large-scale and heterogeneous stress distribution of the 3-m granite/granite laboratory fault facilitate images of the nucleation and growth of dynamic rupture at a variety of locations with respect to the sample boundaries. This added perspective to the longstanding nucleation problem reinforces some previous observations and casts others in a new light. Consistent with past studies, this work demonstrates that the spatial and temporal extent of nucleation is linked and shows how stress levels can systematically affect fault behavior. However, when studying 2-D nucleation effects, it becomes clear that previously reported nucleation phases are likely the result of boundary conditions. Other new observations include nucleation that grows at the transition between creeping and locked fault sections, similar to predictions from numerical studies (e.g., Kaneko & Lapusta, 2008; Tse & Rice, 1986). In other cases, a stuck fault patch within a creeping region becomes a rupture initiation site. At least an order of magnitude variation in apparent L_c is typically observed under nominally similar conditions, and this is further evidence for previously reported loading rate/healing time effects (Guérin-Marthe et al., 2019; Kato et al., 1992; McLaskey & Yamashita, 2017; Xu et al., 2018) and the complicating effects of strength heterogeneity (Harbord et al., 2017; Tal et al., 2018; Ozawa et al., 2019).

Following the Griffith crack concept, most previous studies proposed that L_c is a function of elastic and friction parameters without time dependence. This study suggests that when considering rougher, more heterogeneous natural faults, a time-invariant L_c is not a complete metric for characterizing the initiation of earthquakes and that a parameter with intrinsic time dependence, such as power density (strain energy release per unit time per unit area) is needed (Kaneko et al., 2016). Similarly, the smooth nucleation model of Figure 1 is likely relevant only to unnaturally homogeneous faults. Alternative models of earthquake initiation (Aochi & Ide, 2004) may be more appropriate such as a “cascade up” model (Noda et al., 2013)

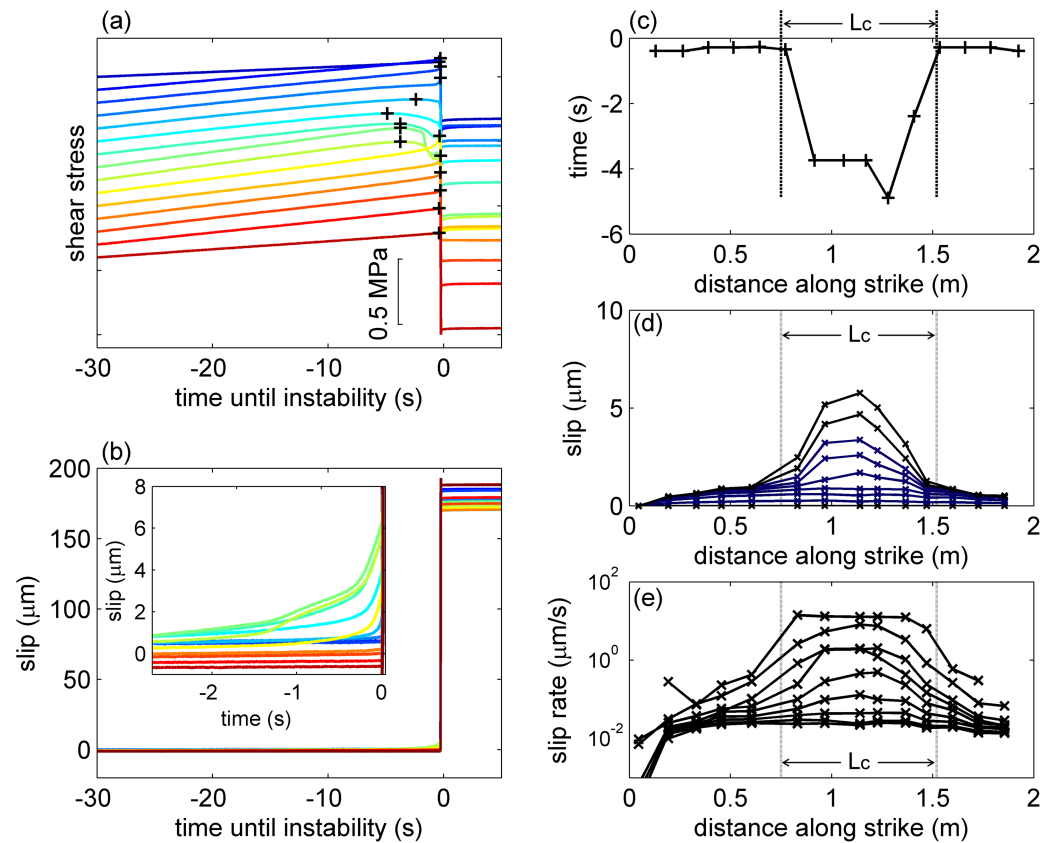


Figure 2. Example nucleation observations on a 2-m rock sample at 6-MPa normal stress. Dynamic rupture is coincident with (a) abrupt drops in local shear stress recorded from a strain gage array and (b) rapid slip recorded with an array of slip sensors. Traces are color coded by sensor position along the length of the 2-m fault and offset for clarity in (a). Crosses in (a) indicate the time of peak stress for each sensor. (c) The crosses are replotted in space-time to estimate critical length scale L_c , similar to Figure 1. (d) Snapshots of the spatial distribution of slip derived from slip data in (b) also provide an image of the nucleation process. Symbols denote measurement locations. (e) Snapshots of slip rate also derived from slip data in (b).

whereby a small brittle fault section can ignite dynamic rupture and circumvent a larger, slower nucleation process.

2. Background on Laboratory Measurements of Slip Initiation

Laboratory samples that contain a sawcut simulated fault often deform in a series of dynamic slip events referred to as “stick-slip” events (Scholz, 2002). The fault remains essentially locked except for sudden episodes of slip that are thought to be representative of earthquakes (Brace & Byerlee, 1966). In many cases, particularly at higher stress levels (40–120 MPa), the initiation of stick-slip events appears to occur abruptly, and the well-defined hypocenter suggests that $L_c < 1$ mm (McLaskey & Lockner, 2014; Passelègue et al., 2013; Thompson et al., 2009).

On larger samples deformed at lower stress levels, details of the initiation process are more easily observed. To illustrate the ways in which nucleation on rock can be observed, one representative stick-slip event from an experiment conducted on the 2-m biaxial apparatus at the USGS, Menlo Park is shown in Figure 2. This event was reported in McLaskey et al. (2015) as DSE13_{May2014}, but it is similar to observations from other laboratories (Kato et al., 1992; Ohnaka & Kuwahara, 1990; Okubo & Dieterich, 1984; Yamashita et al., 2018). The stick-slip event occurs at time $t = 0$ and is characterized by a sudden drop in sample average shear stress supported by the sample and a step-like increase in slip measured on the simulated fault. The sample was instrumented with arrays of sensors that measure local slip and strain gage pairs that measure local shear strain.

2.1. Nucleation Zone

The nucleation zone is an actively slipping region identified by its edge, which can also be described as the crack tip or rupture front. For some transparent glassy polymers, the rupture front can be tracked from changes in stress imaged optically (Guérin-Marthe et al., 2019; Latour et al., 2013; Nielsen et al., 2010; Rosakis et al., 2006). On rock, it is marked by a maximum in a local shear strain measurement (black crosses in Figure 2a) (Dieterich, 1978a; Okubo & Dieterich, 1984) that arises from the stress concentration ahead of an advancing rupture front. Figures 2a and 2c show how arrays of strain gages are used to map rupture fronts in space and time on rock as in Ohnaka and Kuwahara, (1990) and Ohnaka and Shen (1999). The drop in local shear stress is the result of $\sim 1 \mu\text{m}$ of slip in the region. The rupture front can also be estimated from measurements of local fault slip $D(x, t)$ (Figure 2b) by tracking the maximum slip gradient $\partial D/\partial x$ from arrays of sensors (Figure 2d). The slip rate $\dot{D}(x)$, shown in Figure 2e, is relatively constant within the ruptured region but decreases rapidly ahead of the rupture front. The dimensions of the plateau-like $\dot{D}(x)$ curve has been a preferred method for describing characteristics of nucleation in numerical studies (Rubin & Ampuero, 2005), but \dot{D} is difficult to obtain from noisy high-speed laboratory measurements. This study relies primarily on slip measurements similar to Figure 2d to image details of the initiation process.

2.2. Definition of L_c (or h^*)

L_c is defined as the size of the nucleation zone just as it accelerates to seismic slip speeds ($>10 \text{ mm/s}$) and rupture velocities, as described in Figure 1. In this work, L_c refers to both the general concept and the rough measurement shown in Figure 2, not the collection of parameters implied by equation (1). Variations in L_c observed in laboratory experiments need not imply variations in those parameters but instead may highlight complexities not currently captured by equation (1). No distinction is made between L_c and other forms such as L_{sc} , defined as L at the transition from quasistatic to accelerating phases (Ohnaka, 2000) since such definitions may be based on nucleation phases that likely have no counterpart for natural fault rupture (see section 5.3.5). For cases when a more precise definition of L_c is required, the parameter $L_{10\%}$ is used, defined as the ruptured length L (not half length) at the time when dL/dt exceeds $0.1V_s$. Other definitions based on slip rate are described in section 4.5.

Theoretical arguments indicate that L_c has the form

$$L_c = \frac{\alpha G D_c}{\sigma_n f}, \quad (1)$$

where α is a geometric constant of order 1, D_c is the slip weakening distance, σ_n is normal stress, and f is a frictional strength loss. For linear slip weakening friction, Andrews (1976) found $f = (f_0 - f_r)^2 / (f_p - f_r)$, while Campillo and Ionescu (1997) found $f = (f_p - f_r)$. In the previous expressions, f_p is a peak friction level, f_r is a residual friction level, and $f_0 = \tau_0 / \sigma_n$ where τ_0 is an initial shear stress level. For rate- and state-dependent friction, $f = b - a$ is often used (Rice, 1993), though Rubin and Ampuero (2005) showed that f could be as small as $f = (b - a)^2 / (b)$ or as large as $f = b$ (Dieterich, 1992) based on the specifics of the chosen friction constitutive relation and parameters. In the above expressions, b and a are second-order friction parameters with positive values (e.g., $a \approx 0.008$, $b - a \approx 0.02$). Definitions based on different friction equations have been shown to be equivalent under some special conditions (Garagash & Germanovich, 2012; Uenishi & Rice, 2003).

3. Experiments

Experiments were performed on a large-scale direct shear apparatus shown in Figure 3. This machine accommodates a moving rock block and a stationary block that are $3.10 \times 0.81 \times 0.30 \text{ m}$ and $3.15 \times 0.61 \times 0.30 \text{ m}$ in the x , y , and z , directions, respectively. The blocks are composed of Barre granite, and sample surfaces were prepared by the manufacturer to be flat and parallel to $125 \mu\text{m}$. Two sets of hydraulic cylinders were used to apply normal and shear stress to the planar fault that is the $3.10\text{-m} \times 0.3\text{-m}$ interface between the two blocks. A Teflon steel low friction interface is located between the normal loading cylinders and the steel frame (Figure 3b). The moving block and normal loading cylinders can collectively translate in the x direction and slip occurs simultaneously on the dry rock/rock interface and the low friction interface as

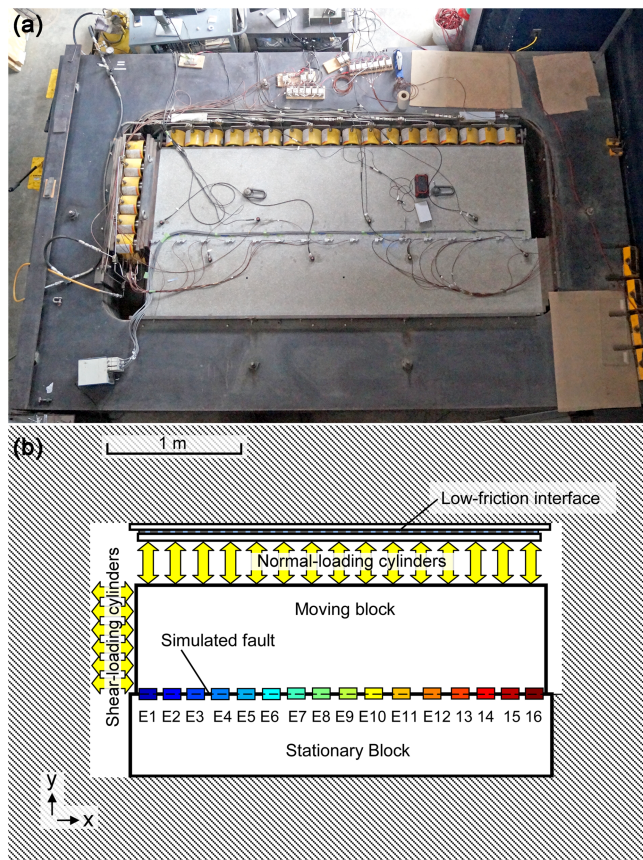


Figure 3. The Cornell 3-m machine. (a) Photograph and (b) schematic diagram show how the granite samples were loaded with 54 hydraulic cylinders within a frame cut from 3-m \times 5-m steel plates. The distribution of fault slip was measured by 16 eddy current displacement sensors that straddle the fault. They detect the dynamic rupture front, preslip during the quasistatic nucleation process, and the slow fault creep that sometimes accumulates during the stick-slip cycle.

described previously (McLaskey & Yamashita, 2017). Prior to the experiments reported in this paper, the samples underwent a run-in period whereby they were forced to slip 15 mm at sample average normal stress $\bar{\sigma}_N = 7$ MPa. Every 40 mm of cumulative slip, the samples were reset by lifting the moving block with a crane. Gouge was not removed. Most of the experiments reported here were conducted after 80 to 120 mm of cumulative slip on the interface.

3.1. Instrumentation

Local fault slip was measured with eddy current sensors at 16 locations equally spaced down the length of the fault and labeled E1–E16 (Figure 3b). These sensors measure the gap between a probe housed in an aluminum holder glued onto the stationary rock block and a target glued to the moving rock block as in McLaskey and Yamashita (2017). The sample average shear stress $\bar{\tau}$ and $\bar{\sigma}_N$ were measured from hydraulic pressure in the shear loading and normal loading sets of cylinders. Measurements from strain gages and piezoelectric sensors were also often collected but are not the focus of this work.

3.2. Loading Procedure

Experiments consisted of runs. For each, the pressure in the normal loading cylinders was increased to a desired level of sample average normal stress $\bar{\sigma}_N$ and then held roughly constant by closing a valve. The pressure in the shear loading cylinders $\bar{\tau}$ was then slowly increased (~ 0.01 MPa/s; ~ 5 $\mu\text{m/s}$) with a hand pump until the fault began to slip spontaneously. Sequences of slip events were generated by continuing to increase $\bar{\tau}$. The first sequence after a large increase in imposed $\bar{\sigma}_N$ produces a specific distribution of $\tau(x)$ and $\sigma_N(x)$ that promotes slip at a location 2 m from the forcing end. This type of sequence was termed a “Poisson” sequence since the stress distribution is partly the result of frustrated Poisson expansion of the sample blocks (Wu & McLaskey, 2019), similar to other sequences generated on plastic samples (Rubinstein et al., 2004). During some sequences, the shear load was occasionally held constant for a set period of time and then resumed at the same rate, in order to test the effects of healing.

4. Results

A general feature of “Poisson” sequences is that the first few slip events rupture only a 1- to 2-m section of the fault centered near E11, 2 m from the forcing end. Successive events progressively rupture larger areas until they rupture through the leading edge of the moving block (red end) and then fully rupture the entire 3.1-m fault. The fully contained events are around $M - 2.5$, slip less than 50 μm , and are often slow (10-mm/s max slip velocity) (Ke et al., 2018). Complete rupture events slip > 100 μm at rates > 0.1 m/s and result in 0.1- to 2-MPa reductions in $\bar{\tau}$.

4.1. Example Sequence at 4 MPa

Figure 4 shows a representative example “Poisson” sequence after $\bar{\sigma}_N$ was increased from 1 to 4 MPa; $\bar{\tau}$ was then increased at about 0.01 MPa/s to rupture the fault at this new, higher, and heterogeneous stress state. The tiny steps in $\bar{\tau}(t)$ are individual pumps of the hydraulic hand pump. As early as time $t = 100$ s, the fault was slowly creeping (~ 100 nm/s) near E12 and E13 (Figure 4c). As early as $t = 170$ s, oscillations in the creep rate could be detected and a sequence of slow slip events of increasing amplitude occurred (Figure 4d). Once these events reached peak slip velocities > 100 $\mu\text{m/s}$, they became significantly more distinct, with slip durations < 2 s and are numbered as dynamic slip events. Successive events have increasing rupture areas, slip speeds, and stress drops.

Figure 5 presents, for each of the 15 events, the distribution of slip measured at all 16 locations along the fault, accumulated in a 1-s time window surrounding the time of peak slip velocity. The first five dynamic

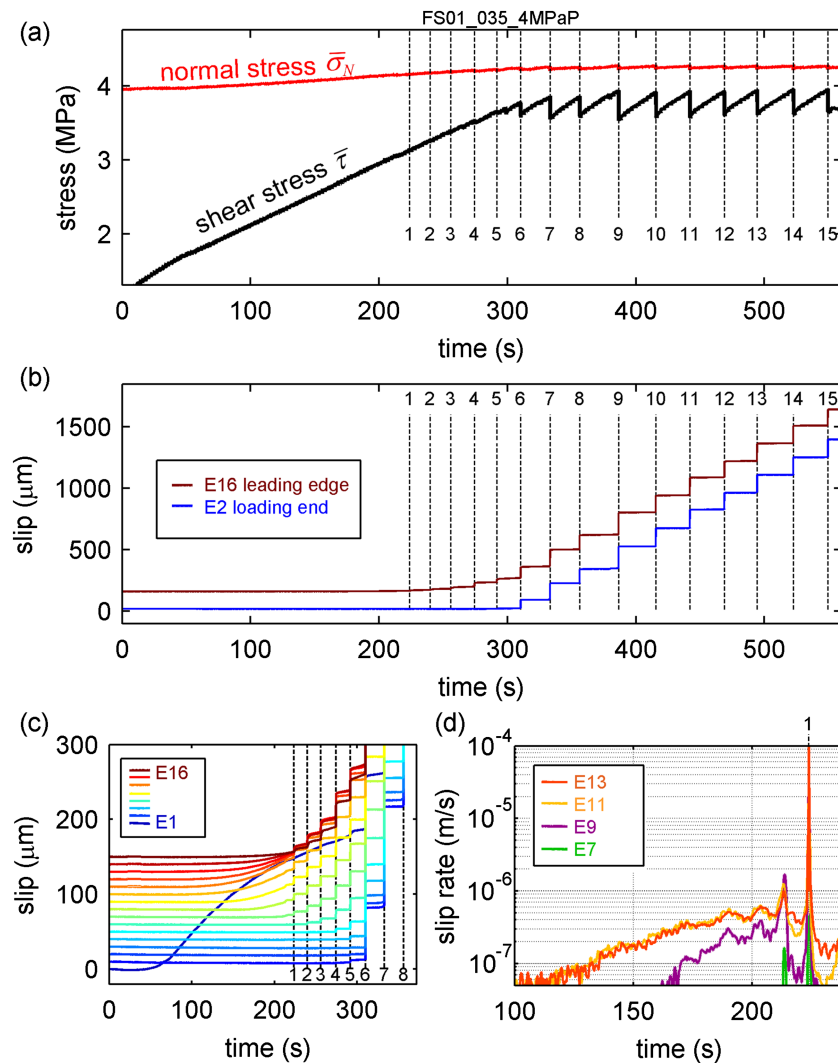


Figure 4. A typical “Poisson” sequence at 4 MPa. (a) $\bar{\sigma}_N$ and $\bar{\tau}$ measured from the hydraulic pressure in the normal loading cylinders and shear loading cylinders, respectively. Dynamic slip events are numbered and labeled with vertical dotted lines. Slip events that do not rupture through the forcing end do not produce the sudden drops in sample average shear stress that are characteristic of standard, complete rupture stick-slip events. (b) Slip measured at the leading edge (E16) and near the loading end (E2) of the sample. Event 6 is the first event to cause slip on both ends. (c) Details of the slip measured by all 16 sensors, offset for clarity. (d) Estimates of slip rate for some of the sensors showing oscillations in the creep rate and a sequence of slow slip events prior to Event 1.

slip events are either fully or partly contained within the 3-m rock sample. Event 6 is the first to rupture the entire interface, yet this event is smaller than later complete rupture events. The contained slip events and the first couple complete rupture events nucleate near $x = 2$ m. Later complete rupture events nucleate near the forcing end, though occasionally the nucleation location can change (section 4.3).

4.2. Summary of Experimental Observations: $\sigma_N = 0.5$ –12 MPa

At 0.5 and 1 MPa, the sample slipped nearly uniformly and slowly. If a long hold period was introduced where the fault could heal in stationary contact, weak stick-slip events could be generated (e.g., Figures 10a–10c). At 2 MPa, the sample could be forced to slip uniformly if loaded rapidly but produced dynamic stick-slip events if loaded at 0.015 MPa/s. At stress levels from 4 MPa up to 12 MPa (the highest tested so far), “Poisson” experiments generated one to five partial rupture events, but the sample soon settled into a regular stick-slip cycle with occasional interseismic partial rupture events localized on the forcing end.

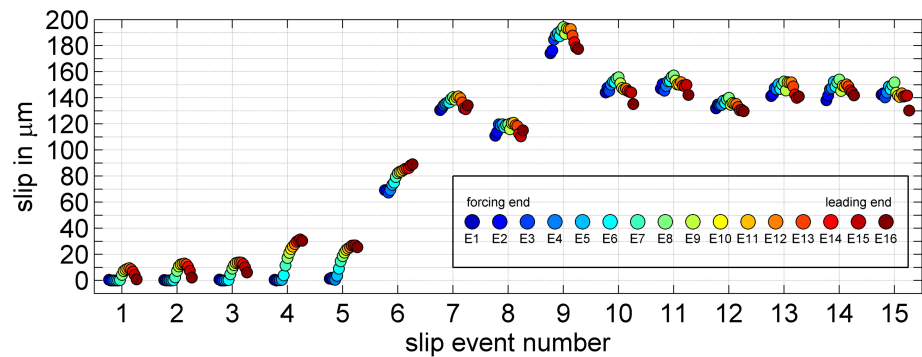


Figure 5. The distribution of slip accumulated in a 1-s time window surrounding each event of the Poisson sequence shown in Figure 4. Blue to red colors denote the measurement location along the length of the 3-m fault (E1–E16, as shown in Figure 3b). Events 1 and 2 are fully confined; Events 3–5 rupture the leading end (red) only. Event 6 is the first to rupture the entire fault. For later events, the sample slips more in the center than at the ends due to a slip deficit built up from interseismic creep at the sample ends.

Consistent with previous reports of stick-slip events, sample-average stress change $\Delta\tau_{\text{mech}}$ measured from complete rupture events was linearly proportional to sample average slip \bar{D} according to $\Delta\tau_{\text{mech}} = k\bar{D}$ where k is the unloading stiffness of the sample/apparatus. Measured $k \approx 1.5$ GPa/m at 2 MPa σ_N and $k \approx 2.6$ GPa/m for 7- to 12-MPa experiments; $\Delta\tau_{\text{mech}}$ and \bar{D} both increase with increasing σ_N , consistent with the idea that $\Delta\mu = \Delta\tau_{\text{mech}}/\sigma_N$ is approximately constant in the σ_N range considered here. The apparent sample average coefficient of friction $\bar{\mu} = \bar{\tau}/\bar{\sigma}$ was 0.8–0.9 for complete rupture events. Taking into account $\bar{\mu}$ of the low friction interface 0.10–0.13 (McLaskey & Yamashita, 2017), the true $\bar{\mu}$ of the rock/rock interface was 0.67–0.80.

4.3. Imaging the Initiation of a Slip Event

For each slip event of a sequence, the nucleation process was imaged from slip sensor measurements E1–E16. Figure 6 shows data recorded from Event 10, which is a typical event from the sequence shown in Figures 4 and 5 and is very similar to Events 7, 8, and 11–15. Event 9, the largest event of the sequence, is shown in Figure 7. Its initiation was different from most other complete rupture events.

The event shown in Figure 6 initiated near the forcing end ($x = 0.5$ m) and the slowly slipping nucleation region expanded as it accelerated. It was about 1.5 m in size when V_r exceeded $0.1V_s$, marked by the vertical dotted line ($V_s = 2,700$ m/s was assumed). A small amount of slow fault creep can be seen near the leading edge of the fault ($x > 2.3$ m). For Event 9, shown in Figure 7, both ends of the 3-m fault were slowly creeping at about $1 \mu\text{m/s}$, while the central meter of the fault was essentially locked. A localized patch of accelerating slip centered near $x = 2$ m developed near the edge of the creeping region. This patch, which could be considered the nucleation zone or the shear crack, grew to about 1 m in size and then rapidly accelerated to rupture velocities at a significant fraction of V_s .

4.4. The 2-D Effect

Figure 8 shows a representative event at $\bar{\sigma}_N = 7$ MPa in an experiment where the slip sensors were placed on both the top and bottom fault traces of the granite slab to give some insight into the 2-D effect. Slip maps made from only the top (Figure 8a) and bottom (Figure 8b) sensors show different one-dimensional views of the same 2+-D process (similar to Figures 6a, 7a, and 10). These results indicate that $L_c \approx 0.8$ m can be roughly estimated from either data set since it is substantially longer than the 0.3-m slab thickness.

The 2-D nucleation process, interpolated from top and bottom measurements, is shown in Figure 8c. This shows that slow slip $< 1 \mu\text{m/s}$ started near the bottom surface and quickly accelerated to $\sim 100 \mu\text{m/s}$ when the expanding slip front breached the top free surface. Slip accumulated on the top surface for a few milliseconds, then, propagating along the full thickness of the sample, it quickly accelerated to seismic speeds approaching V_s .

The sudden increase in slip rate observed near the top surface at $-0.005 > t > -0.002$ suggests that interaction between an expanding slow slipping region and a free surface stimulates slip acceleration. These 2-D

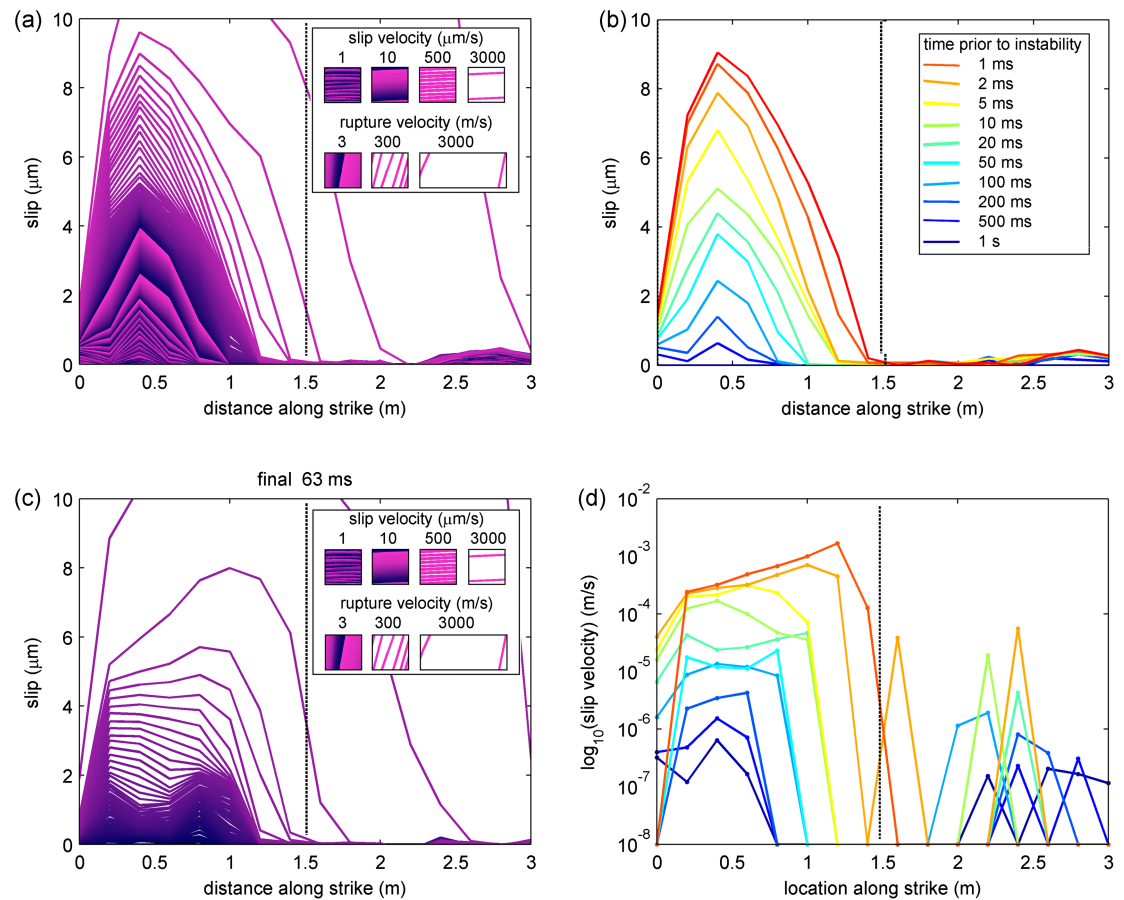


Figure 6. The initiation of Event 10 from the sequence shown in Figures 4 and 5 imaged from slip measurements four different ways. (a) Slip contours are drawn every 200 μm . The contour colors cycle from light pink to dark purple every 0.1 s. Color banding indicates slow creep $\sim 1 \mu\text{m/s}$. Stretched banding indicates slip rates 10–100 $\mu\text{m/s}$. Separation of individual contours occurs at weakly seismic slip rates of 1 mm/s. The horizontal spacing of contours is proportional to the rupture velocity. (b) Logarithmically spaced slip contours. Constant contour spacing indicates that slip velocity increases as $1/t_f$ where $t_f = t_{\text{in}} - t$ is the time until instability. (a) and (b) show slip relative to slip at time $t = t_{\text{in}} - 2 \text{ s}$. (c) same as (a) but the slip is plotted relative to slip at time $t = t_{\text{in}} - 0.063 \text{ s}$. (d) Slip rate estimated from average slip during the log-spaced time intervals shown in (b). Slip rates $> 10^{-5} \text{ m/s}$ on the right side of the figure are likely artifacts due to noise.

effects cause perturbations in the nucleation process widely recognized as nucleation phases (see section 5.3.5). Observations from other laboratories corroborate with this 2-D view of the nucleation process. For a similar experimental setup on a 1.5-m rock sample, Xu et al. (2018) showed how nucleation tends to occur near either the top or bottom free surface, where stiffness is lower. Fukuyama et al. (2018) used a 2-D strain gage array embedded within the sample to track nucleation and showed that rupture usually initiates at free surfaces but can also initiate within the slab by coalescence of multiple slow slip regions. McLaskey and Kilgore (2013) also described nucleation phases resulting from 2-D effects.

4.5. Nucleation Length $L_{10\%}$

To further study quantitative details of nucleation, the actively slipping zone (ASZ) was first defined as the region on the fault where at least 1 μm of slip occurred in the 63 ms prior to instability (i.e., slip rates $> 15 \mu\text{m/s}$). The rupture front is the edge of the ASZ. This definition helped separate nucleation-related slow slip from slow constant creep ($\sim 1 \mu\text{m/s}$ rates). The time of instability was determined as the time when slip rate on any part of the fault exceeded either 3 mm/s ($t_{3\text{mm/s}}$, with corresponding size of ASZ $L_{3\text{mm/s}}$) or 10 mm/s ($t_{10\text{mm/s}}$, $L_{10\text{mm/s}}$) or, alternatively, as the time when one of the two rupture fronts exceeded 10% of V_s ($t_{10\%}$, $L_{10\%}$) (Kaneko & Lapusta, 2008). To track the rupture front, $t_{\text{front}}(x)$ was defined as the time when 1 μm of slip had accumulated relative to the slip measured 63 ms prior to dynamic

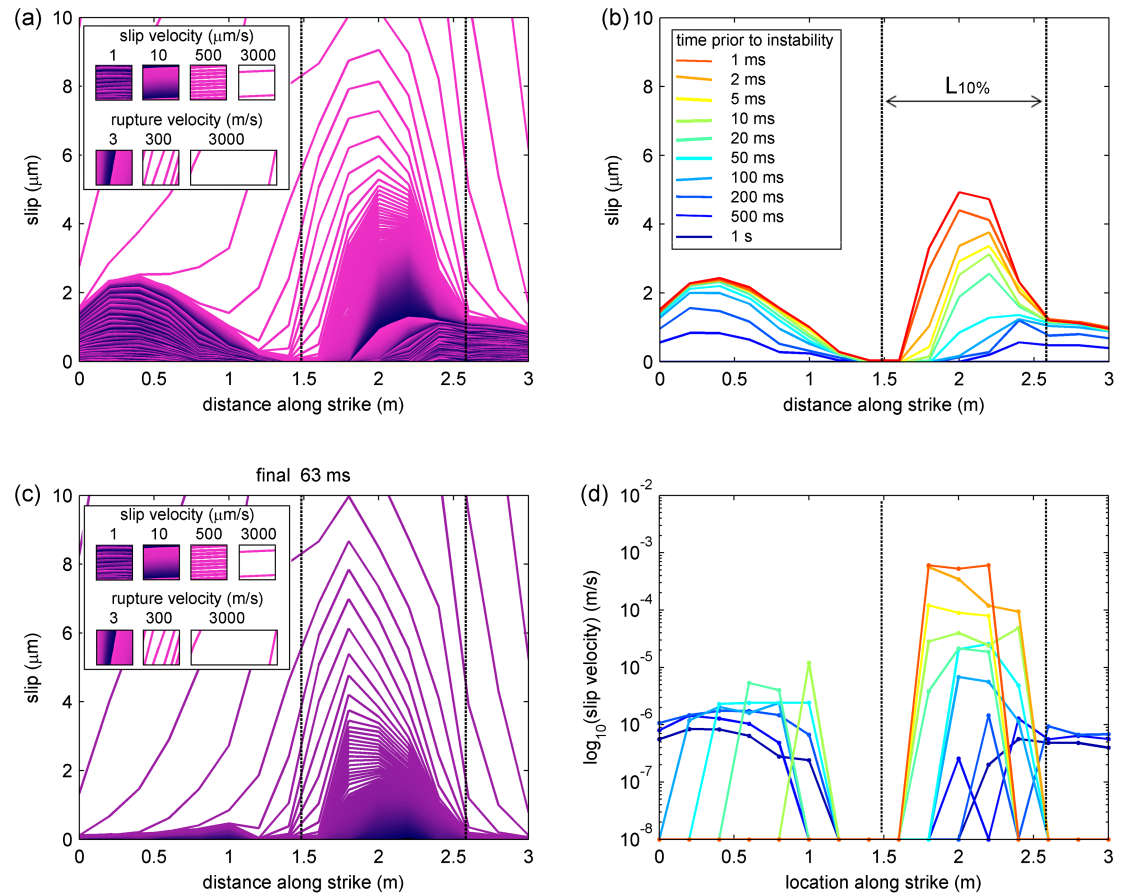


Figure 7. The initiation of Event 9 from the sequence shown in Figures 4 and 5 imaged from slip measurements. All panels are similar to Figure 6. This event initiates more abruptly in space and time near the edge of a creeping region near $x = 2$ m. Different from the event of Figure 6, this event does not accelerate as smoothly and slip velocity does not increase as $1/t_f$.

rupture. The speed of the expanding front $V_r = |(\partial t_{\text{front}}(x)/\partial x)^{-1}|$. For most of the events studied, the $1\text{-}\mu\text{m}$ threshold and 63-ms time window could be varied by a factor of 3 without strong effect on $L_{10\%}$ estimates.

Figure 9 shows $L_{10\text{mm/s}}$, $L_{3\text{mm/s}}$, and $L_{10\%}$ determined for 105 slip events generated at a range of σ_N . The $1/\sigma_N$ trend predicted by equation (1) is shown by diagonal lines in Figure 9. The maximum observable L_c was limited by the 3-m length of the block and L_c estimates smaller than the 0.3-m thickness of the granite slab cannot be accurately resolved due to 2-D effects. To minimize edge effects, the only events included were those where the ASZ did not include either the end of the sample end ($L_{3\text{mm/s}}$, $L_{10\text{mm/s}}$) or both of the two rupture fronts accelerated to 10% V_s ($L_{10\%}$). As a result, many events with larger nucleation or nucleation near the forcing end were not included in the 105 events shown in Figure 8.

The three definitions of L_c ($L_{10\text{mm/s}}$, $L_{3\text{mm/s}}$, and $L_{10\%}$) were consistent to about a factor of 3; however, $L_{10\%}$ was typically larger than $L_{3\text{mm/s}}$, smaller than $L_{10\text{mm/s}}$, and more closely matched $L_{3\text{mm/s}}$ for most of the events studied. $L_{10\text{mm/s}}$ showed somewhat less variability than the others and more closely matched the rough estimates of L_c reported in Figure 11, which are based on the observations of Figure 10. Large $L_{10\%}$ was never observed at high σ_N , yet small $L_{10\%}$ was observed even at low σ_N .

4.6. Presentation of 15 Random Events

To present a set of observations that are free from selection bias, 15 slip events were chosen at random from all experiments conducted with consistent instrumentation. The initiation processes of those 15 random events are shown in Figure 10. These events exemplify general trends in sample behavior and also illustrate some of the commonly observed complexities.

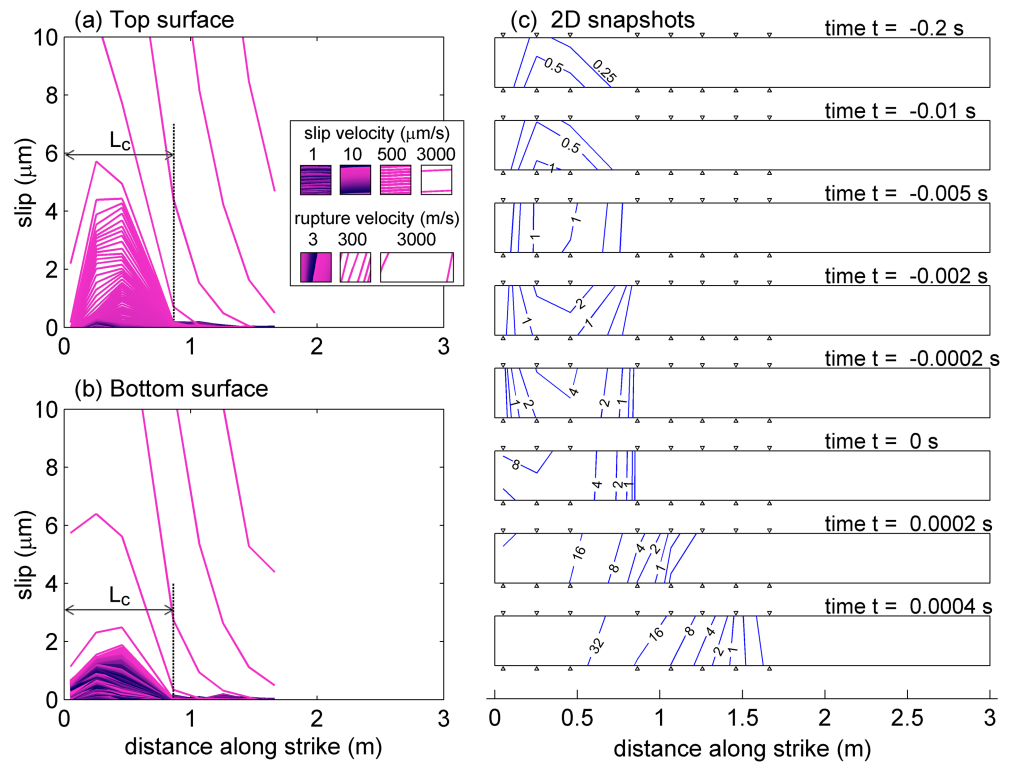


Figure 8. The 2-D effects of nucleation. The images on the left were generated from slip data on the top (a) and bottom (b) surfaces of the granite slab. Slip snapshots are drawn every 100 μs , and all plotting characteristics are identical Figures 6a and 7a. (c) Slip contours drawn on the fault cross section at various snapshots in time t , relative to the initiation of dynamic rupture; contours are labeled in micrometers of slip, and the locations of the 16 slip sensors are shown as triangles. The comparison in (a) and (b) shows that $L_c \approx 0.8$ m can be roughly estimated from either data set. Differences between them illustrate the 2-D effects of nucleation. The slow slip occurs preferentially on one free surface or the other. Slow fault creep first occurred near the bottom of the slab for a few hundred milliseconds, but about 7 ms before dynamic rupture, the top surface started to slip at a faster rate, which accelerated to dynamic rupture through the full thickness of the granite slab.

The majority of events nucleated near the forcing end. The exceptions were (i) events that occurred after occasional interseismic partial rupture events (Figure 10o), (ii) contained events resulting from the perturbed stress state of Poisson experiments (Figure 10g), and (iii) events generated at low normal stress ≤ 2 MPa where most of the fault exhibited creep and initiation occurred on a stuck patch (Figures 10b and 10c), as described in section 5.3.3.

A marked difference in behavior was observed as a function of σ_N . At $\sigma_N < 4$ MPa, meter-sized sections of the fault could creep at $\sim 1\text{-}\mu\text{m/s}$ rates. These extended creeping patches were far less common at 7 and 10 MPa since they soon became unstable and ruptured dynamically.

5. Discussion

5.1. Comparison of L_c With Other Studies

Figure 11 shows L_c estimates from this work against those from previous laboratory experiments conducted on both rock samples and glassy polymers. The red circles are rough estimates of L_c determined from the events of Figure 10. Pairs of symbols at a given σ_n give some indication of representative ranges. However, these rough estimates exclude events generated after an imposed hold period that initiated more rapidly and with smaller apparent L_c (Figures 10a, 10k, 10m, and 10n), as described in section 5.2.

Some bounds on L_c may also be determined from the stability threshold of stick-slip to stable sliding of a slider block loaded in a stiff machine where the sample is the most compliant element (Dieterich,

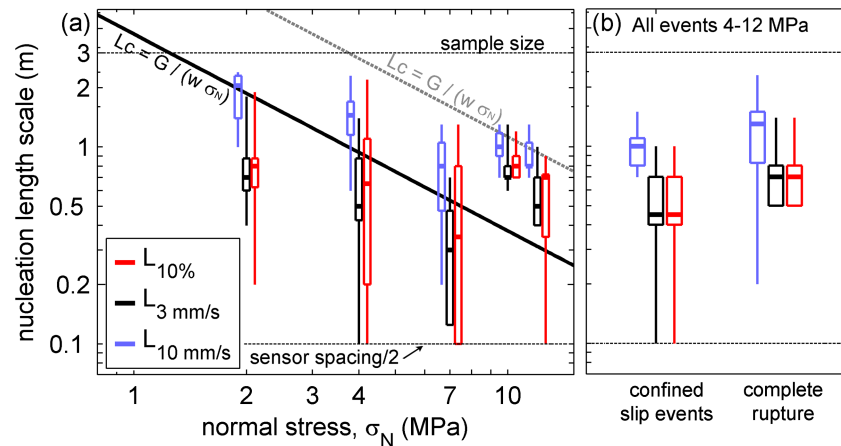


Figure 9. Parametric quantification of the nucleation process for a collection of 105 slip events. The critical length scale is quantified in three different ways ($L_{10\%}$, $L_{3\text{mm/s}}$, and $L_{10\text{mm/s}}$, see text). These metrics are (a) shown against σ_N and (b) used to compare complete rupture events to partial rupture events. All results are shown as box and whisker plots made from groups of estimates. The box extends from the 25th to 75th percentiles of the data with a thick bar at the 50th percentile, and the whiskers indicate the full range. The observable range is bounded by the sample size (3 m) and half the sensor spacing (0.1 m) shown as horizontal dotted lines. The diagonal lines show the expected variation in L_c from equation (1), where $w = f/(\alpha D_c)$. At higher σ_N , large $L_{10\%}$ was not observed, suggesting that the upper bound of $L_{10\%}$ may be controlled by the expected $L_c \sim 1/\sigma_N$ relationship (diagonal lines). At lower normal stress, more than an order of magnitude variation in $L_{10\%}$ was observed.

1978b; McLaskey & Yamashita, 2017). If a sample of length L_{sample} with a velocity weakening frictional interface slides stably, it is safe to assume that $L_c > L_{\text{sample}}$. If the same sample undergoes slow slip events, then $L_c \approx L_{\text{sample}}$. If $L_c < L_{\text{sample}}$, then the sample will likely exhibit dynamic stick-slip events. These constraints are shown as triangles connected by horizontal dotted lines in Figure 11.

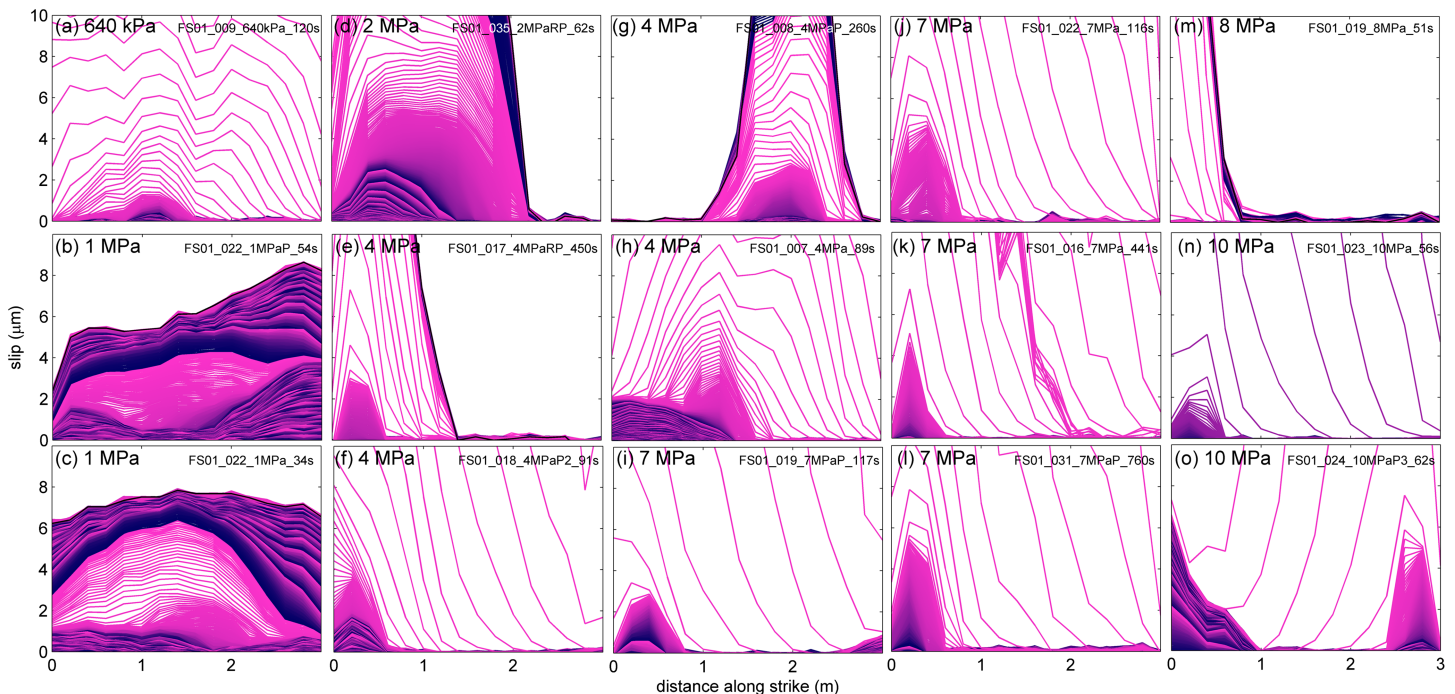


Figure 10. Nucleation characteristics of 15 randomly selected events. Each panel shows slip snapshots from 2 s before to 1 s after the start of each slip event. Snapshots are drawn every 100 μs , and all plotting characteristics are identical to Figures 6a, 7a, 8a, and 8b. The events are organized by $\bar{\sigma}_N$: (a) 670 kPa, (b, c) 1 MPa, (d) 2 MPa, (e–h) 4 MPa, (i–l) 7 MPa, (m) 8 MPa, (n, o) 10 MPa.

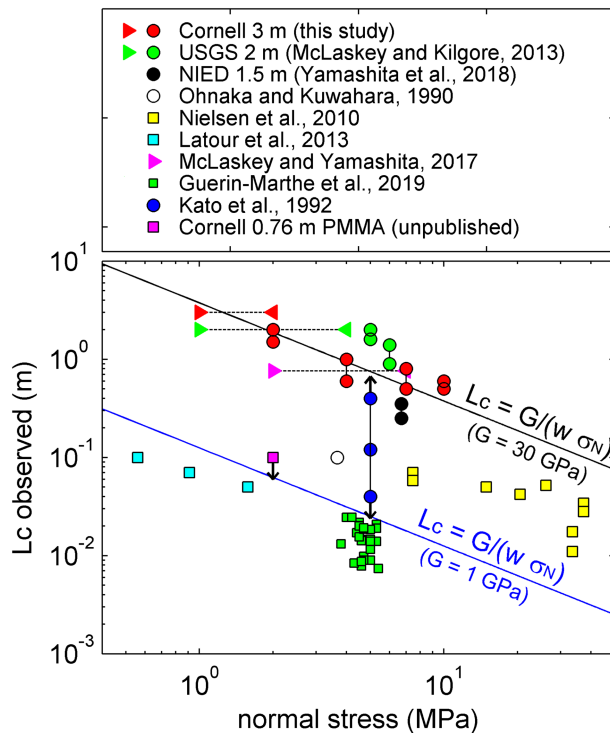


Figure 11. Comparison of laboratory observations of L_c across many studies. Square symbols indicate experiments conducted on glassy polymers, while circles are those on rocks. Triangles connected by horizontal dotted lines indicate constraints based on a stick-slip versus steady-sliding sample behavior threshold. The USGS 2-m block is likely somewhat rougher than others, while Onaka and Kuwahara, (1990) is smoother. Variability due to loading rate effects is shown in Kato et al. (1992) and Guérin-Marthe et al. (2019).

5.1.3. Normal Stress

Nucleation models also indicate $L_c \propto \sigma_N^{-1}$. Most studies in Figure 11 show the expected inverse relation between L_c and σ_N , though it is poorly constrained due to limited range in σ_N . In the current study, overall sample behavior of stick-slip versus steady sliding is consistent with $L_c \sim \sigma_N^{-1}$ trends. The results of Figure 9 show that $L_{10\%}$ is essentially independent of σ_N , though there is a suggestion that the maximum $L_{10\%}$ may be controlled by a $1/\sigma_N$ relationship (gray diagonal dotted line). Harbord et al. (2017) showed a complicated dependence of sample behavior on σ_N , possibly due to changes in wear processes at different stress levels.

5.2. Loading Rate/Healing Time

L_c has been shown to shrink with increasing loading rate in laboratory experiments (Guérin-Marthe et al., 2019; Kato et al., 1992; Xu et al., 2018) and in numerical studies using rate- and state-dependent friction equations (Kaneko et al., 2016; Kaneko & Lapusta, 2008). Consistent with earlier modeling (Gu et al., 1984), McLaskey and Yamashita (2017) showed that this effect occurs if a fault section is “kicked” far above steady state either by suddenly increasing loading rate or upon resumption of loading after the fault is held in essentially stationary contact. (Note that if the loading machine is stiff enough, a high but constant loading rate will not induce a “kick.” It will instead push the sample closer to steady state and the opposite effect will be observed.) The reduction in L_c induced by kicks suggests that kicks increase the rate of fault weakening or brittleness of the fault. This effect has been shown by some laboratory rock experiments (Chang et al., 2012; Kato et al., 1992; Liao et al., 2014; Xu et al., 2018). When modeled using the rate and state frameworks, this “kick”-dependent phenomena is likely sensitive to the “aging law” versus “slip law” formulation (Ampuero & Rubin, 2008; Bhattacharya & Rubin, 2014).

The trend lines in Figure 11 show expected L_c from equation (1) assuming $w = f/(\alpha D_c) = 8,000$ and representative G for rock and plastic, as indicated. The trend line was chosen to roughly fit most of the data, and the values of the underlying parameters ($D_c = 2 \mu\text{m}$, $f = .012$, $\alpha = 0.77$) are roughly consistent with friction parameters expected for bare rock surfaces.

5.1.1. Elastic Modulus of Fault Rocks/Forcing Blocks

Equation (1) indicates $L_c \propto G$. Consistent with this trend, smaller L_c was observed on plastic samples (squares in Figure 11, $G \approx 1 \text{ GPa}$) than on rock (circles, $G \approx 30 \text{ GPa}$). On the compliant plastic material, dynamic instability can develop over centimeter length scales even at 1 MPa stress levels, whereas many meters of a stiffer rock sample would be required for a similar instability to develop. This is the advantage of using analog materials to study post-nucleation rupture processes (Rosakis et al., 2006; Rubinstein et al., 2004).

5.1.2. Fault Surface Roughness

Rougher samples and those with increased gouge layer thickness have larger D_c (Marone & Kilgore, 1993) and should exhibit larger L_c (equation (1)). Consistent with this expectation, experiments on roughened samples show larger L_c (Ohnaka & Shen, 1999; Okubo & Dieterich, 1984) or more stable sample behavior (Dieterich, 1978b). These experiments were conducted on samples that had been ground flat and then roughened to produce uniform surface topography with a specified roughness that may not be representative of natural fault surfaces. More recently, Yamashita et al. (2018) studied progressive roughening from continued sliding of a 1.5-m sample and found more variation and complexity in the initiation process for the roughest samples. The current work on the Cornell 3-m machine indicated that progressively smaller L_c and more dynamic stick-slip events were generated during the initial run-in period, consistent with similar observations on bare granite samples (McLaskey & Lockner, 2018) and a reduction in D_c observed during evolution of gouge layers (Scuderi et al., 2017).

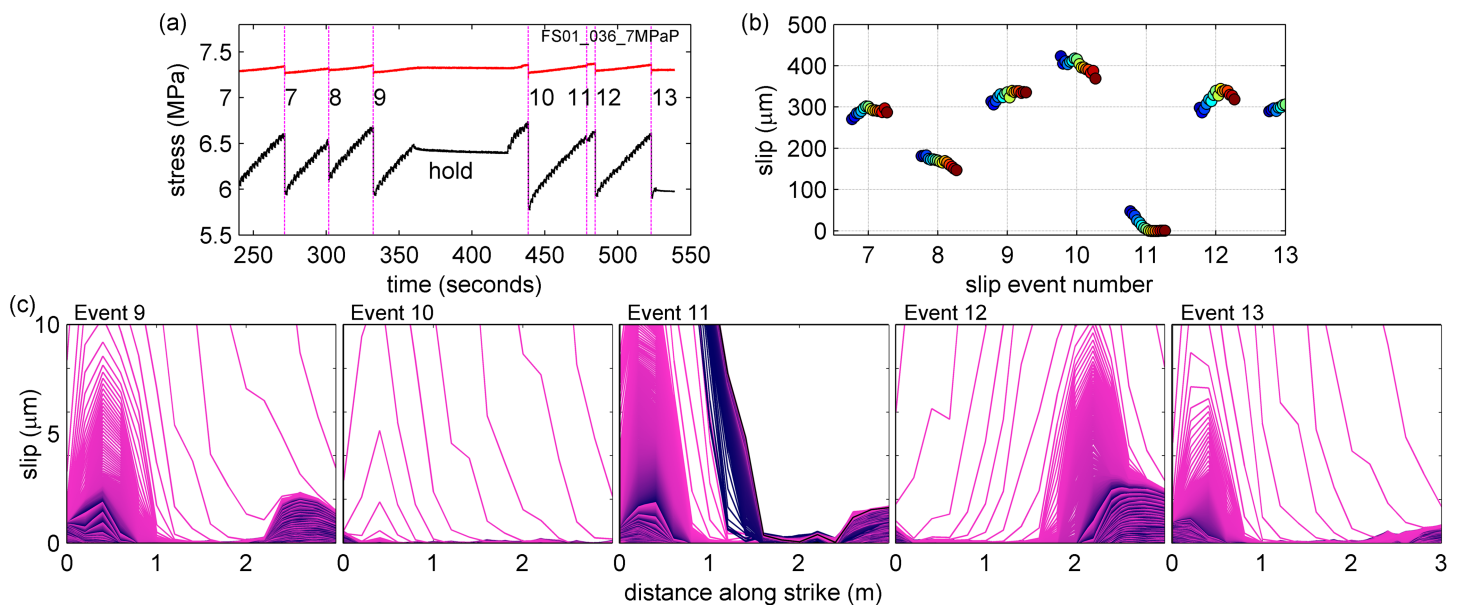


Figure 12. Example sequence with a hold showing “kick”-induced nucleation effects and variable nucleation locations. (a) Loading data for this sequence with event numbers labeled, similar to Figure 4a. (b) Slip distribution data for each event, similar to Figure 5. (c) Images of the nucleation of five different events, slip snapshots are drawn every 100 μs , and all figure properties identical to those in Figures 6a, 7a, 8a, 8b, and 10. This sequence illustrates two effects: (1) Nucleation size and speed are affected by the hold, as evidenced by the abrupt initiation of Event 10, and (2) the nucleation location is affected by the distribution of stress along the fault: Event 11 relieved stress only on the forcing end and this pushed the nucleation of Event 12 to the opposite end of the sample.

In this study, the fault was kicked above steady state by imposing a hold period where loading rate was set to 0. This technique was particularly effective when the hold was imposed near a critical stress level (i.e., sample average shear stress $\bar{\tau} > 0.9 \bar{\tau}_{\text{max}}$) since it minimized slow slip prior to the subsequent dynamic rupture. As an illustrative example, a $\sigma_N = 7.3\text{-MPa}$ run is shown in Figure 12. Event 9 nucleated in a 1-m-sized zone near the loading end of the sample, similar to most events of the sequence. Loading rate was set to 0, the sample was held for about 60 s, and then loading was resumed. The initiation of the next event (#10) was more sudden and with a smaller apparent L_c . Creep was suppressed. L_c was less than 100 mm (the minimum detectable with the sensor array), at least 5 times smaller than typical. Nucleation was also more abrupt. Slip rate reached seismic speeds after less than 0.5 μm of prior slip, 20 times smaller than the 10 μm of slip that was typically needed to achieve seismic speeds. The events of Figures 10a, 10k, 10m, and 10n also occurred after holds. Most of these events initiated more rapidly than events on the same experimental run that were not preceded by a hold.

One might suggest that the apparent reduction in L_c is actually the result of a 2-D effect—that the nucleation location moved to within the slab rather than near the top surface where it would be detected. However, the “kick”-dependent reduction in L_c was consistently observed during a variety of experiments at a variety of stress levels and at multiple locations along the fault, so it is more likely that nucleation truly became smaller and more abrupt. It is possible that 2-D effects, interactions with heterogeneity, and other factors not yet accounted for can complicate this effect, as discussed below.

5.3. Effects of Heterogeneity

Growing evidence indicates that natural faults have spatial variation in both strength and stress. Variation in coseismic earthquake slip inferred from kinematic inversion suggests heterogeneous stress changes during both large (Hartzell & Heaton, 1983) and small earthquakes (Dreger et al., 2007). This could arise from roughness of the fault surfaces found to exist at a variety of scales (Brown & Scholz, 1985; Candela et al., 2012). Fault roughness may, in turn, promote variation in fault rheology such as velocity weakening fault patches surrounded by velocity strengthening regions. Spatial streaking of small earthquakes (e.g., Rubin et al., 1999) and repeating earthquake sequences (e.g., Nadeau & Johnson, 1998; Vidale et al., 1994) also suggest heterogeneous fault properties.

Heterogeneity is a key part of an increasing number of numerical models relevant to earthquake initiation (e.g., Hillers et al., 2006; Luo & Ampuero, 2018; Ray & Viesca, 2017; Skarbek et al., 2012; Tal et al., 2018). Studies that include creeping sections show nucleation that preferentially occurs at the transition between creeping and locked fault sections (Kaneko & Lapusta, 2008; Tse & Rice, 1986) or due to the coalescence of creeping fronts on a 2-D fault (Chen & Lapusta, 2009; Kaneko & Ampuero, 2011; Schaal & Lapusta, 2019).

5.3.1. Nucleation at the Transition Between Creeping and Locked

In the current laboratory work, the entire 3-m fault will creep at $<1\text{-}\mu\text{m/s}$ rates at low $\sigma_N < 2$ MPa, but with continued wear, the two ends of the fault have become more prone to creep over time even at $\sigma_N = 7\text{--}12$ MPa. The two ends carry higher normal stress and show heavy wear, compared to the occasional striation in the center section of the fault. Creep near the fault ends became more prevalent after resetting the sample suggesting that reorganization of the gouge layer is partly responsible. On the other hand, creep was reduced or inhibited by hold periods, as discussed in section 5.2.

Similar to the above numerical simulations, nucleation frequently occurred at the transition between creeping and locked fault sections, as shown in Figures 7, 10h, and 12c, Event 12. Subsequent dynamic rupture ensued bilaterally, with somewhat faster rupture speed into the locked region than back over the creeping region.

5.3.2. Location of Nucleation and Ignition

Heterogeneity can influence the location of nucleation in complex ways. Typically, slip has been observed to initiate at the maximum of $\tau(x)/\sigma_N(x)$ (Ben-David et al., 2010; Yamashita et al., 2018). Laboratory samples typically have a normal stress distribution that is bowl shaped, with higher normal stress near the sample ends (Kammer et al., 2015; Ke et al., 2018; Xu et al., 2019; Yamashita et al., 2018). In this case, if shear stress is applied uniformly, nucleation starts at the center of the sample where $\sigma_N(x)$ —and fault strength—is lowest. If the sample is loaded from one end, nucleation occurs close to where it was loaded, where τ is high.

The above observations suggest that, if $\tau(x)$ is uniform enough, earthquakes will initiate where faults are weakest, since Coulomb friction suggests that strength is proportional to σ_N . However, sometimes earthquakes appear to initiate on strong patches. For example, some events generated on the 2-m biaxial apparatus at the USGS, Menlo Park, appear to initiate at one end of the 2-m fault where σ_N is higher and the fault is stronger (McLaskey et al., 2015, Figure 3b). The sample edge is relatively strong due to locally high σ_N , and once this strong edge slips, it causes a sudden slip acceleration that can sometimes ignite dynamic rupture. Yet slower fault slip always initiated in the center of the fault (McLaskey & Kilgore, 2013) where it was weakest. So, while rupture of the stronger sample edge is what initiated dynamic rupture, this stronger fault patch was loaded to failure primarily from the expanding slow slipping region that began at the weaker fault section. Measurement techniques in both the laboratory and field (e.g., Gueren Marthe et al., 2019; Johnston et al., 2006) may be blind to $1\text{-}\mu\text{m/s}$ slow slip in the very early stages of nucleation and focus only on the final ignition of dynamic rupture.

This complexity requires us to distinguish between nucleation and ignition, as illustrated in Figure 13. The figure presents a simplified conceptual sketch of a heterogeneous fault with fault patches that are mildly weaker or stronger than their surroundings. Here “weak” and “strong” are intended to be characterized by comparatively lower and higher effective normal stress, respectively, that might result naturally from interacting topography of the fault surfaces. The model is an extreme simplification since size, shape, spacing, and intensity of the heterogeneity can all influence the resulting slip. Additionally, as noted previously, strength alone does not determine where a fault slips (instead, it is $\tau(x)/\sigma_N(x)$), yet to simplify the discussion, it is assumed here that $\tau(x)$ is uniform enough that $\sigma_N(x)$ is the primary contributor to heterogeneity and that the heterogeneity is mild enough that there is little overall variation in L_c . (If the heterogeneity was strong, each patch would have its own L_c .)

In the model of Figure 13, slow slip associated with nucleation always begins on weak fault sections, but both strong and weak fault patches can be the apparent ignition site for dynamic rupture (orange in Figure 13). Figure 13a shows a case where L_c is small compared to the length scale of the heterogeneity, and most of the fault is locked. In this “slip limited” environment, nucleation initiates at a weaker section of the fault, once slow slip expands to an L_c -sized region similar to the schematic in Figure 1. In the opposite case, shown in Figure 13b, L_c is large compared to the length scale of the heterogeneity, most of the fault creeps, and dynamic rupture initiates near a strong patch due to a “kick”-dependent transient reduction

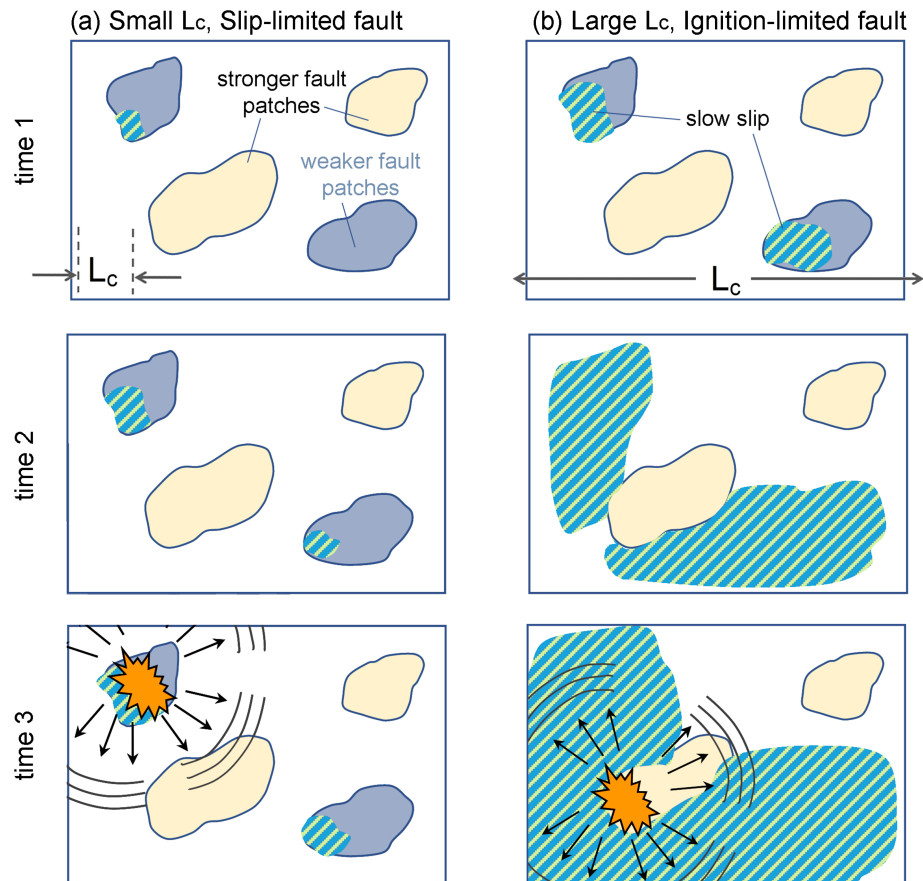


Figure 13. Schematic diagram of earthquake initiation on a heterogeneous fault. (a) When L_c is small compared to the relevant scale of strength heterogeneity, most of the fault is locked and an earthquake initiates on a weaker fault patch once the size of the quasistatically slipping region exceeds L_c , consistent with Figure 1. (b) When L_c is larger than the scale of heterogeneity, earthquake initiation occurs on a strong fault patch where stress and stressing rate concentrate, different from the model of Figure 1.

in L_c . This case is denoted an “ignition-limited” environment since the fault is more readily able to creep but may have trouble transitioning to or “igniting” dynamic rupture. In an “ignition-limited” environment, dynamic rupture initiation occurs not because a slipping region exceeds a time-invariant critical length scale, but because the strain energy release per unit time per unit area exceeds a critical breakdown power density (Kaneko et al., 2016). Stress concentrations due to slip surrounding a locally strong fault patch, or perhaps the sudden rupture of the strong patch, can be sufficient sources of power.

5.3.3. Initiation at a Stuck Patch—Cascade Up

The sudden acceleration of slip due to the rupture of a small brittle fault patch can hasten dynamic rupture and shrink the earthquake initiation process in space and time. This effect is known as “cascade up” (Noda et al., 2013). Figure 14 illustrates laboratory observations of a similar effect. This sequence of three consecutive events was conducted at $\sigma_N = 2$ MPa, and in all three cases, most of the fault creeps. Panels on the right side of Figure 14 show slip time history recorded by the slip sensor located closest to the center of the nucleation (near $x = 1.3$ m) and the gray dotted line shows a $1/t_f$ reference line ($t_f = t_{in} - t$ is the time until instability). The event of Figures 14a and 14b show a smooth nucleation process with $L_{10\%} \approx 1.5$ m. Figure 14b shows that slip increased as $1/t_f$. The two subsequent events in the sequence initiated more abruptly in space and time ($L_{10\%} < 0.5$ m) and slip near the center of the nucleation zone accelerates faster than the $1/t_f$ model (Figures 14d and 14f). Those two events initiated near a section of the fault that was essentially locked and not creeping, which is referred to here as a stuck patch. This shows that when the stuck patch does finally rupture, it accelerates the nucleation process. Other evidence of this effect can be seen in McLaskey and Kilgore (2013) Figure 10 and Zhuo et al. (2018) Figure 3a.

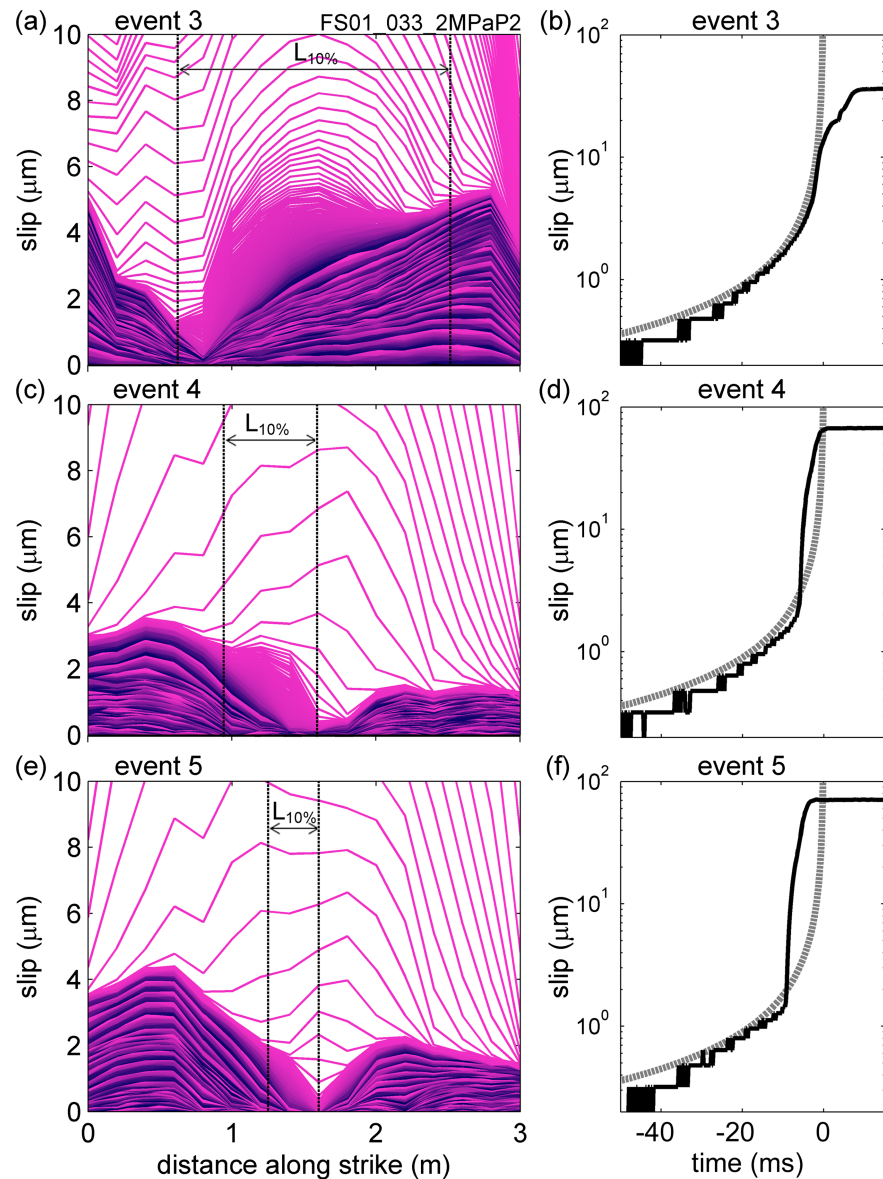


Figure 14. Observation of cascade up from a sequence of three consecutive events. Panels on the left show slip snapshots that describe the initiation of dynamic rupture. Snapshots are drawn every $100 \mu\text{s}$ and all plotting parameters are identical to Figures 6a, 7a, and 10 and others. Vertical dotted lines indicate the locations where $V_r > 0.1V_s$, used to estimate critical length scale $L_{10\%}$. Panels on the right show the slip time history measured by the slip sensor located closest to the center of nucleation, near $x = 1.3 \text{ m}$. The gray dotted line shows a $1/t_f$ reference line (see text). (The step-like character of the slip measurements below $1 \mu\text{m}$ is an artifact of quantization.) These three events show that the 1.5-m large nucleation observed in (a, b) that has slip consistent with $1/t_f$ can be circumvented by the sudden rupture of a smaller stuck patch, as shown in (c, d) and (e, f).

Different from the model of Noda et al. (2013), the results of Figure 14 show that the stuck patch does not have remarkably different properties from the surrounding fault. The location of the stuck patch is not constant. This and the overall smooth nature of the laboratory fault indicate that very slight variations in strength can cause the differences in earthquake initiation shown in Figure 14. When the stuck patch happens to slide into existence, it is nominally stronger than the surrounding fault, is locked or slips slower than its surroundings, and is therefore rapidly loaded by slip of the surrounding fault sections. The sudden increase in loading rate “kicks” the stuck patch, and the mechanism described in section 5.2 causes the patch to fail more brittlely and unstably. The same “kick”-induced embrittlement can act again when the stuck patch finally ruptures and rapidly delivers the built-up stress back to the surrounding fault. This rapid

stress transfer can push the surrounding fault above steady state and make it more brittle and susceptible to continued dynamic rupture. On natural faults, stronger brittle patches may develop naturally over time through strain localization (e.g., Scuderi et al., 2017).

5.3.4. Multiscale Strength Heterogeneity

Faults have roughness at a wide range of length scales (e.g., Brown & Scholz, 1985; Candela et al., 2012), and this may also imply strength heterogeneity at a range of length scales, which has strong implications for the manner in which earthquakes initiate. If multiscale strength heterogeneity was added to Figure 13a, then within each of the weak and strong patches would exist smaller subpatches of weaker and stronger fault sections. That smaller-scale heterogeneity would be smaller than L_c , similar to Figure 13b. In other words, if one were to zoom in on the weak patch which hosts the initiation of dynamic rupture in Figure 13a, the process would look similar to the ignition-limited nucleation process of Figure 13b. Consequently, faults with multiscale strength heterogeneity should host earthquakes that initiate with a rate-dependent process (Figure 13b) that is better characterized by a critical power density (Kaneko et al., 2016) than a critical length scale L_c . If correct, the nucleation model of Figure 1 is an attribute of unnaturally flat faults with nearly uniform properties and would not be appropriate for naturally rough faults. Hierarchical models (Aochi & Ide, 2004; Ide & Aochi, 2005) would be more appropriate, especially if they include rate-dependent effects.

5.3.5. Nucleation Phases

Laboratory studies often highlight different nucleation phases (i.e., quasistatic and acceleration) (Ohnaka & Kuwahara, 1990; Ohnaka & Shen, 1999), yet numerical studies that employ homogeneous fault properties describe smooth, progressive acceleration of the nucleation region without such phases (e.g., Dieterich, 1992; Dublanchet, 2018; Rubin & Ampuero, 2005). This work and other evidence (Dieterich, 1978a; Fukuyama et al., 2018; McLaskey & Kilgore, 2013) show that different stages are likely due to interactions of slow slip fronts with free surfaces either at the sample ends or at the top and bottom of the slab, as described section 4.4. This type of free surface-induced variation in the nucleation process has no natural counterpart since natural earthquakes initiate at depth; however, both natural and laboratory faults likely contain heterogeneous stress or strength, and the laboratory observations of nucleation phases further demonstrates the importance of this heterogeneity during the earthquake initiation process.

5.4. Nucleation Versus Termination

Some studies have explored whether nucleation characteristics affect the eventual size of an earthquake (e.g., Beroza & Ellsworth, 1996; Lapusta & Rice, 2003). In the current experiments, there are many cases where two events nucleated in nearly identical locations with similar conditions, yet one event went on to rupture the entire 3-m fault and the other terminated prematurely (see, e.g., Figure 10e vs. Figure 10f or Figure 12 Event 9 vs. Event 11). Within the uncertainty of these observations (2-D effects), there are no obvious differences in their nucleation processes, and this suggests that stress conditions even just a few L_c away from the location of nucleation have no effect on the nucleation process. Two events that nucleate identically could become vastly different earthquakes as the expanding dynamic rupture encounters different stress conditions. Figure 9b shows that $L_{10\text{mm/s}}$, $L_{3\text{mm/s}}$, and $L_{10\%}$ estimates are somewhat larger for complete rupture events than for confined events; however, the differences are small compared to the overall variation in L_c .

5.4.1. Abrupt Initiation Causes More Powerful Rupture

As illustrated in sections 5.2 and 5.3, there can be considerable variation in how events initiate, and this study clearly shows that events that initiate more abruptly are more powerful than events that have larger nucleation. For example, the event shown in Figure 14a with a large nucleation slipped only about 36 μm , while the subsequent events slipped 65 and 69 μm . Similarly, for the sequence shown in Figures 4 and 5, Event 9 has the smallest nucleation zone and it also slipped more and faster than neighboring events. These observations suggest that earthquakes that initiate more abruptly with smaller L_c have more intense stress concentrations at the edges of their ruptures, have larger dynamic stress drops, and would thus produce larger earthquakes if other fault properties are identical. In contrast, an earthquake that initiates sluggishly spends more of its budget for moment release on slow slip. Further descriptions about how variations in nucleation affect stress drop, maximum slip velocity, and radiated seismic waves are presented in Wu and McLaskey (2019). However, the strength of the above effect may be exaggerated in the laboratory where L_c is a significant fraction of the total sample size. Differences in the initiation process may have a smaller effect on large earthquakes with rupture areas much larger than L_c .

6. Scaling Up to Natural Faults

L_c is not well constrained in nature; no laboratory-like earthquake nucleation measurements have been achieved in the field. In a few cases, upper bounds on L_c have been made from borehole strain measurements (e.g., Johnston et al., 2006), but this disqualifies only nucleation zones larger than 10 km and only at specific fault locations. Instead, seismic measurements such as foreshocks, tremors, and initial P wave signatures primarily shape our understanding of earthquake initiation (Bouchon et al., 2011, 2013; Chen & Shearer, 2013; Dodge et al., 1995; Ellsworth & Bulut, 2018; Kato et al., 2012; Ruiz et al., 2017; Tape et al., 2018). A coalescence of seismicity is sometimes observed (Savage et al., 2017) in a source volume near the eventual hypocenter of a larger earthquake. This section discusses how the laboratory results might inform the initiation of larger earthquakes on natural faults and the interpretation of foreshocks. Two endmember models of small and large nucleation are presented along with their implications. The third model, which merges aspects of each endmember, is guided by the laboratory observations and suggests that heterogeneity and rate-dependent variability in nucleation work together to produce a rate-dependent “cascade up” process.

6.1. Cascade Model: Small Nucleation on the Order of a Meter

In this model, it is assumed that L_c is smaller than the source dimension of the smallest seismicity recorded. Thus, $L_c \leq 1$ m for $M - 2$ events, and possibly $L_c \leq 100$ mm for $M - 4$ mine seismicity (Boettcher et al., 2009; Kwiitek et al., 2010). The fault is locked with essentially no aseismic slip. This scenario may be expected throughout much of the seismogenic zone on continental faults that host intraslab earthquakes and many interslab events.

Considering equation (1), $L_c \sim 0.1\text{--}1$ m requires $D_c \sim 3\text{--}30$ microns, which is consistent with laboratory values for faults with minimal fault gauge. In this calculation, it is assumed that $\sigma_N = 100$ MPa and $f = b - a = 0.008$, the maximum found by Blanpied et al. (1995) for wet granite gouge at seismogenic pressures and temperatures.

With regard to foreshocks, small L_c suggests a “cascade” foreshock model, as described schematically in Figure 15b. In this case, there are no differences—other than size—between small foreshocks and larger earthquakes. They nucleate similarly, and a large earthquake is simply a small earthquake that happened to encounter fault conditions favorable for continued rupture. Any quasistatic nucleation is likely tens of centimeters in size at most and occurs in milliseconds, similar to laboratory observations. Foreshocks may smooth the along-fault stress distribution and allow for a larger rupture (Ke et al., 2018).

A cascade model may also be correct if the concept of L_c and the model presented in Figure 1 is easily superseded by some other brittle process that can ignite earthquakes (grain crushing or buckling of force chains) and is not considered by standard friction constitutive equations.

The cascade model cannot account for extended creeping regions seen on many faults, described in the next section. It may also have trouble accounting for delayed dynamic triggering, which suggests a temporally extended nucleation process, which is less likely with small L_c .

6.2. Preslip Model: Large Nucleation on the Order of Kilometers

A large L_c allows for extended aseismic slip. Geodetic observations and small, regularly repeating earthquake sequences provide evidence for aseismic slip on at least some faults including oceanic transform faults (McGuire et al., 2012), many subduction zones (Johnson et al., 2016; Uchida et al., 2012), and some mature faults such as sections of the San Andreas fault (e.g., Linde et al., 1996).

Considering equation (1), $L_c \geq 10$ km can be achieved with f negative (velocity strengthening) or close to 0. Earthquakes cannot nucleate on such fault sections since $L_c \rightarrow \infty$. This case is expected at the deepest extent of crustal faults near the brittle-plastic transition where tectonic tremor has been observed (Bürgmann, 2018). Velocity strengthening or nearly velocity neutral behavior is also reported in laboratory experiments on unconsolidated gouge layers, talc, and many clay materials (e.g., Ikari et al., 2011). These conditions are also expected in the shallowest parts of subduction zones including those targeted in some drilling programs that sample fault sections that are known to creep (e.g., Carpenter, et al., 2016; Saffer & Wallace, 2015).

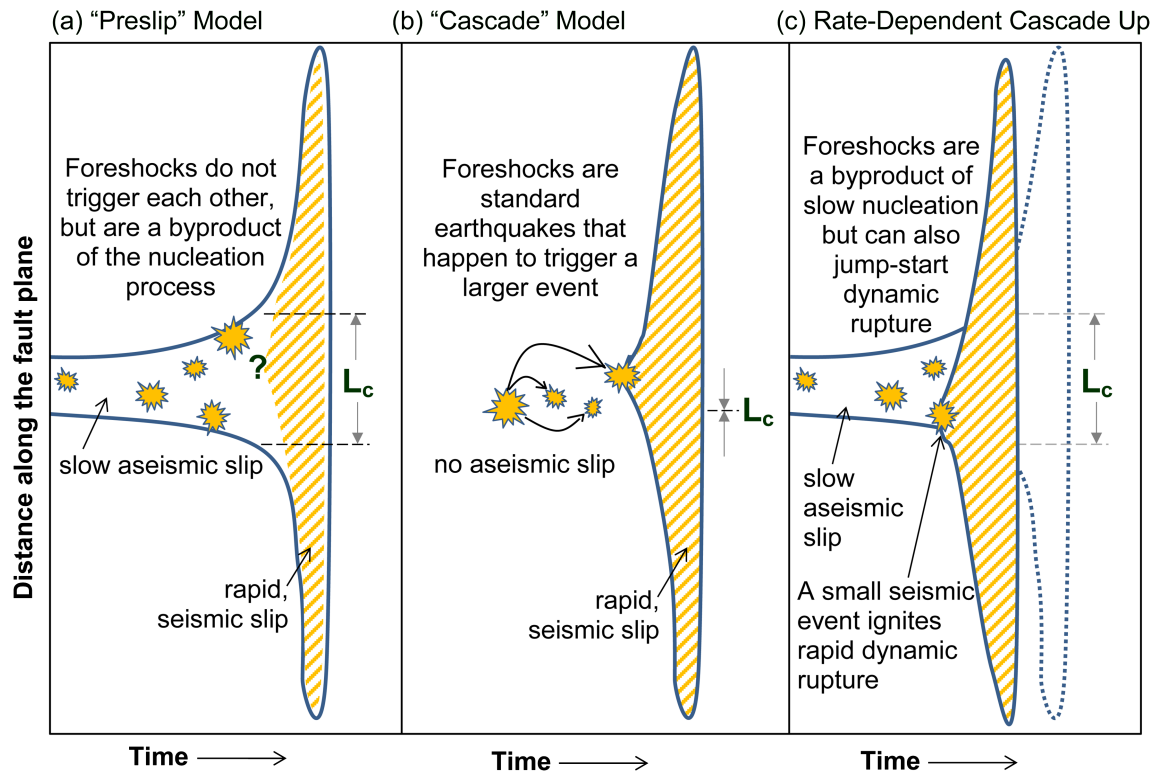


Figure 15. Three earthquake initiation models, their relationship to L_c , and their implications for foreshocks. The preslip model (a) and cascade model (b) illustrate endmember behavior where L_c is large (>10 km) or small (<1 m). (c) The laboratory observations suggest a rate-dependent cascade up model, which contains attributes of both endmembers.

Alternatively, if f is closer to laboratory values for granite, then a large D_c on the order of 0.1 to 1 m is needed to produce $L_c \sim 10$ km. Ohnaka (2000) argued that D_c (and also L_c) scales with the size of an earthquake and $D_c \approx 1$ m for larger earthquakes. However, this argument was based primarily on seismic observations (Ellsworth & Beroza, 1995) and remains debated.

Large L_c suggests a “preslip” foreshock model, described schematically in Figure 15a. In this model, small earthquakes are fundamentally different from larger ones, even if those differences cannot be ascertained from their seismic source parameters. The nucleation of large earthquakes is dictated by an effective L_c , based on a large-scale spatial average of fault properties. Smaller earthquakes, with rupture dimensions smaller than the effective L_c (termed “sub- L_c ” or “sub- h^* ” events), require heterogeneous fault properties for their existence. They occur on small fault patches that are more brittle (and have locally smaller L_c) than their surroundings (Noda et al., 2013; McLaskey & Kilgore, 2013; Schall and Lapusta, 2019).

In this model, foreshocks are a by-product of a large nucleation process, and the spatial extent of foreshock clusters provides some indication of the effective L_c . This may explain foreshock sequences observed before some recent subduction zone earthquakes (Brodsky & Lay, 2014; Kato et al., 2012; Ruiz et al., 2017).

Under the preslip model, the precise beginning of a large earthquake is unclear (question mark in Figure 15a). The model might imply an accelerating crescendo of seismicity or an emergent initiation of seismic waves. However, other than a few notable cases (Bouchon et al., 2011; Tape et al., 2013; Tape et al., 2018), such observations are rarely reported. This model also has trouble accounting for observations that small and large earthquakes initiate and grow similarly (McLaskey & Lockner, 2014; Okuda & Ide, 2018; Uchide & Ide, 2010).

6.3. Rate-Dependent Cascade Up Model Assisted by Variable L_c

The two above cases are endmembers, and many models exist that merge the attributes of each. For example, Noda et al. (2013) presented a heterogeneous model with small brittle fault patches with small L_c surrounded

by fault sections with larger L_c . In this model, brittle patches can rupture to create small events that, in some cases, ignite dynamic rupture in the surrounding fault and cause larger ruptures without a large nucleation. The model presented here is similar, but there is no requirement for strong heterogeneity. Instead, a large variation in L_c can develop naturally as a result of mild strength heterogeneity and loading rate effects described in section 5.2.

The implications of this model are described in Figure 15c. L_c can be large, allowing for extended creeping regions. Like the preslip model, foreshocks are “sub- h^* ” events that occur only because they are “kicked” by nucleation-related aseismic slip. Yet every foreshock that occurs kicks the surrounding fault, tests its local strength and stability, and threatens to ignite a much larger rupture (McLaskey & Lockner, 2014). In this way, swarms of seismicity driven by aseismic slip are possible, but when considering initial P wave signatures, small and large earthquakes can appear to initiate similarly.

7. Conclusion

This study presents images of the initiation of dynamic rupture made from local fault slip measurements on a 3-m granite fault. Many ruptures initiated in a manner consistent with the smooth nucleation model shown in Figure 1 with a well-defined critical length scale L_c . The fault was essentially locked (slipping less than 100 nm/s), and slow slip on one section of the fault accelerated and grew until it rapidly transitioned to dynamic rupture velocities. In these cases, the dependence of L_c on normal stress and rigidity of the rock generally followed trends expected from theory. In other cases, part of the fault was creeping at a nearly steady rate of $\sim 1 \mu\text{m/s}$, and a nucleation region similar to that described above developed at the intersection of the creeping and locked fault segments. These experiments also showed that nucleation phases are the result of 2-D effects and free surface boundary conditions, the nucleation process can be independent of termination conditions just a few L_c away, and events with smaller and more abrupt nucleation tend to produce more powerful ruptures.

However, two effects observed here indicate that the smooth nucleation model of Figure 1 may poorly describe the initiation of earthquakes on naturally rough faults. First, this work adds to accumulating evidence suggesting that “kicks” above steady state can shrink the spatial and temporal extent of the nucleation process. For example, an experiment that imposed a 60-s hold where the loading rate was set to 0 and then resumed at the same rate was enough to reduce apparent nucleation length by about an order of magnitude. Second, stress concentrations that arise as a result of fault strength heterogeneity were also shown to cause dynamic rupture to initiate more abruptly and with smaller apparent L_c . This was seen in cases where most of the fault could slowly creep and dynamic rupture was observed to initiate at the location of a stuck patch: a fault section mildly stronger than the surrounding fault.

L_c (or h^*) is often considered to be a constant that characterizes a particular fault based on the (time-invariant) elastic and frictional properties described in equation (1). In contrast, the above laboratory observations argue that the earthquake initiation process and the apparent L_c can vary strongly over time (indeed, over a single earthquake cycle) due to “kick”-dependent effects. The laboratory observations further show that this variability in apparent L_c is enhanced by mild heterogeneity of fault properties. As a result, naturally heterogeneous faults may produce earthquakes whose initiation is different from the smooth nucleation model of Figure 1, and a time-invariant L_c is likely an incomplete metric for characterizing initiation. A parameter with intrinsic rate dependence, such as power density (Kaneko et al., 2016), is likely needed. Many faults around the world are not entirely locked and can host slow fault slip. This work suggests that, on those faults, earthquakes will ignite if local fault slip redistributes strain energy at a rate that exceeds a critical power density, potentially at a length scale far smaller than the effective L_c derived from spatially averaged fault properties.

References

- Ampuero, J.-P., & Rubin, A. M. (2008). Earthquake nucleation on rate and state faults—Aging and slip laws. *Journal of Geophysical Research*, 113, B01302. <https://doi.org/10.1029/2007JB005082>
- Andrews, D. J. (1976). Rupture velocity of plane strain shear cracks. *Journal of Geophysical Research*, 81(32), 5679–5687. <https://doi.org/10.1029/jb081i032p05679>
- Aochi, H., & Ide, S. (2004). Numerical study on multi-scaling earthquake rupture. *Geophysical Research Letters*, 31, L02606. <https://doi.org/10.1029/2003GL018708>

Acknowledgments

This work was supported by National Science Foundation Grant EAR-1645163. Data used in this paper were acquired during laboratory experiments conducted at Cornell University. Data reported here are publicly available online (<https://eCommons.cornell.edu>). C.-Y. Ke and B. S. Wu assisted with the experiments. T. Bond, A. Reid, B. S. Wu, D. McLaskey, and T. Brock assisted with the construction of the 3-m apparatus. J. Mangus and the synchrotron crew kindly assisted with unloading the steel frame. K. Keranen provided grant writing mentorship and helpful conversations that lead to Figure 15. N. Beeler and P. Bhattacharya provided comments on an early version of the manuscript. J.-P. Ampuero and an anonymous reviewer provided helpful comments that improved this paper. All authors declare that they have no conflict of interest.

- Ben-David, O., Cohen, G., & Fineberg, J. (2010). The dynamics of the onset of frictional slip. *Science*, 330(6001), 211–214. <https://doi.org/10.1126/science.1194777>
- Beroza, G. C., & Ellsworth, W. L. (1996). Properties of the seismic nucleation phase. *Tectonophysics*, 261, 209–227. [https://doi.org/10.1016/0040-1951\(96\)00067-4](https://doi.org/10.1016/0040-1951(96)00067-4)
- Bhattacharya, P., & Rubin, A. M. (2014). Frictional response to velocity steps and 1-D fault nucleation under a state evolution law with stressing-rate dependence. *Journal of Geophysical Research: Solid Earth*, 119, 2272–2304. <https://doi.org/10.1002/2013JB010671>
- Blanpied, M. L., Lockner, D. A., & Byerlee, J. D. (1995). Frictional slip of granite hydrothermal conditions. *Journal of Geophysical Research*, 100, 13045–13064. <https://doi.org/10.1029/95jb00862>
- Boettcher, M. S., McGarr, A., & Johnston, M. (2009). Extension of Gutenberg-Richter distribution to Mw–1.3, no lower limit in sight. *Geophysical Research Letters*, 36, L10307. <https://doi.org/10.1029/2009GL038080>
- Bouchon, M., Durand, V., Marsan, D., Karabulut, H., & Schmittbuhl, J. (2013). The long precursory phase of most large interplate earthquakes. *Nature Geoscience*, 6, 299–302. <https://doi.org/10.1038/ngeo1770>
- Bouchon, M., Karabulut, H., Aktar, M., Özalaybey, S., Schmittbuhl, J., & Bouin, M.-P. (2011). Extended nucleation of the 1999 Mw 7.6 Izmit earthquake. *Science*, 331(6019), 877–880. <https://doi.org/10.1126/science.1197341>
- Brace, W. F., & Byerlee, J. D. (1966). Stick-slip as a mechanism for earthquakes. *Science*, 153, 990–992. <https://doi.org/10.1126/science.153.3739.990>
- Brodsky, E. E., & Lay, T. (2014). Recognizing foreshocks from the 1 April 2014 Chile earthquake. *Science*, 344(6185), 700–702. <https://doi.org/10.1126/science.1255202>
- Brown, S. R., & Scholz, C. H. (1985). Broad bandwidth study of the topography of natural rock surfaces. *Journal of Geophysical Research, Solid Earth*, 90(B14), 12,575–12,582. <https://doi.org/10.1029/jb090ib14p12575>
- Bürgmann, R. (2018). The geophysics, geology and mechanics of slow fault slip. *Earth and Planetary Science Letters*, 495, 112–134. <https://doi.org/10.1016/j.epsl.2018.04.062>
- Campillo, M., & Ionescu, I. R. (1997). Initiation of antiplane shear instability under slip dependent friction. *Journal of Geophysical Research*, 102(B9), 20,363–20,371. <https://doi.org/10.1029/97jb01508>
- Candela, T., Renard, F., Klinger, Y., Mair, K., Schmittbuhl, J., & Brodsky, E. E. (2012). Rough-ness of fault surfaces over nine decades of length scales. *Journal of Geophysical Research, Solid Earth*, 117(B8). <https://doi.org/10.1029/2011jb009041>
- Carpenter, B., Ikari, M., & Marone, C. (2016). Laboratory observations of time-dependent frictional strengthening and stress relaxation in natural and synthetic fault gouges. *Journal of Geophysical Research: Solid Earth*, 121, 1183–1201. <https://doi.org/10.1002/2015JB012136>
- Chang, J. C., Lockner, D. A., & Reches, Z. (2012). Rapid acceleration leads to rapid weakening in earthquake-like laboratory experiments. *Science*, 338(6103), 101–105. <https://doi.org/10.1126/science.1221195>
- Chen, T., & Lapusta, N. (2009). Scaling of small repeating earthquakes explained by interaction of seismic and aseismic slip in a rate and state fault model. *Journal of Geophysical Research*, 113, B01311. <https://doi.org/10.1029/2008jb005749>
- Chen, X., & Shearer, P. M. (2013). California foreshock sequences suggest aseismic triggering process. *Geophysical Research Letters*, 40, 1–6. <https://doi.org/10.1029/2012GL054022>
- Dieterich, J. H. (1978a). Preseismic fault slip and earthquake prediction. *Journal of Geophysical Research*, 83(B8), 3940–3948. <https://doi.org/10.1029/jb083ib08p03940>
- Dieterich, J. H. (1978b). Time-dependent friction and the mechanics of stick-slip. *Pure and Applied Geophysics*, 116(4-5), 790–806. <https://doi.org/10.1007/BF00876539>
- Dieterich, J. H. (1992). Earthquake nucleation on faults with rate- and state-dependent friction. *Tectonophysics*, 211, 115–134. [https://doi.org/10.1016/0040-1951\(92\)90055-b](https://doi.org/10.1016/0040-1951(92)90055-b)
- Dodge, D. A., Beroza, G. C., & Ellsworth, W. L. (1995). Foreshock sequence of the 1992 Landers, California, earthquake and its implications for earthquake nucleation. *Journal of Geophysical Research*, 100, 9865–9880. <https://doi.org/10.1029/95jb00871>
- Dreger, D., Nadeau, R. M., & Chung, A. (2007). Repeating earthquake finite source models: Strong asperities revealed on the San Andreas fault. *Geophysical Research Letters*, 34, L23302. <https://doi.org/10.1029/2007GL031353>
- Dublanche, P. (2018). The dynamics of earthquake precursors controlled by effective friction. *Geophysical Journal International*, 212(2), 853–871. <https://doi.org/10.1093/gji/ggx438>
- Ellsworth, W., & Beroza, G. C. (1995). Seismic evidence for an earthquake nucleation phase. *Science*, 268(5212), 851–855. <https://doi.org/10.1126/science.268.5212.851>
- Ellsworth, W. L., & Bulut, F. (2018). Nucleation of the 1999 Izmit earthquake by a triggered cascade of foreshocks. *Nature Geoscience*, 11(7), 531–535. <https://doi.org/10.1038/s41561-018-0145-1>
- Fang, Z., Dieterich, J. H., & Xu, G. (2010). Effect of initial conditions and loading path on earthquake nucleation. *Journal of Geophysical Research*, 115, B06313. <https://doi.org/10.1029/2009JB006558>
- Fukuyama, E., Tsuchida, K., Kawakata, H., Yamashita, F., Mizoguchi, K., & Xu, S. (2018). Spatiotemporal complexity of 2-D rupture nucleation process observed by direct monitoring during large-scale biaxial rock friction experiments. *Tectonophysics*, 733, 182–192. <https://doi.org/10.1016/j.tecto.2017.12.023>
- Garagash, D. I., & Germanovich, L. N. (2012). Nucleation and arrest of dynamic slip on a pressurized fault. *Journal of Geophysical Research*, 117, B10310. <https://doi.org/10.1029/2012JB009209>
- Gu, J. C., Rice, J. R., Ruina, A. L., & Simon, T. T. (1984). Slip motion and stability of a single degree of freedom elastic system with rate and state dependent friction. *Journal of the Mechanics and Physics of Solids*, 32(3), 167–196. [https://doi.org/10.1016/0022-5096\(84\)90007-3](https://doi.org/10.1016/0022-5096(84)90007-3)
- Guérin-Marthe, S., Nielsen, S., Bird, R., Giani, S., & Di Toro, G. (2019). Earthquake nucleation size: Evidence of loading rate dependence in laboratory faults. *Journal of Geophysical Research: Solid Earth*, 124(1), 689–708. <https://doi.org/10.1029/2018JB016803>
- Harbord, C. W., Nielsen, S. B., De Paola, N., & Holdsworth, R. E. (2017). Earthquake nucleation on rough faults. *Geology*, 45(10), 931–934. <https://doi.org/10.1130/g39181.1>
- Hartzell, S. H., & Heaton, T. H. (1983). Inversion of strong ground motion and teleseismic waveform data for the fault rupture history of the 1979 Imperial Valley, California, earthquake. *Bulletin of the Seismological Society of America*, 73(6A), 1553–1583.
- Hillers, G., Ben-Zion, Y., & Mai, P. M. (2006). Seismicity on a fault controlled by rate- and state-dependent friction with spatial variations of the critical slip distance. *Journal of Geophysical Research*, 111, B01403. <https://doi.org/10.1029/2005JB003859>
- Ide, S., & Aochi, H. (2005). Earthquakes as multiscale dynamic ruptures with heterogeneous fracture surface energy. *Journal of Geophysical Research*, 110, B11303. <https://doi.org/10.1029/2004JB003591>
- Ikari, M. J., Marone, C., & Saffer, D. (2011). On the relation between fault strength and frictional stability. *Geology*, 39(1), 83–86. <https://doi.org/10.1130/G31416.1>

- Johnson, K. M., Mavrommatis, A., & Segall, P. (2016). Small interseismic asperities and widespread aseismic creep on the northern Japan subduction interface. *Geophysical Research Letters*, 43, 135–143. <https://doi.org/10.1002/2015GL066707>
- Johnson, T. L., & Scholz, C. H. (1976). Dynamic properties of stick-slip friction of rock. *Journal of Geophysical Research*, 81(5), 881–888. <https://doi.org/10.1029/JB081i005p00881>
- Johnston, M. J. S., Borchardt, R. D., Linde, A. T., & Gladwin, M. T. (2006). Continuous borehole strain and pore pressure in the near field of the 28 September 2004 M 6.0 Parkfield, California, earthquake: Implications for nucleation, fault response, earthquake prediction, and tremor. *Bulletin of the Seismological Society of America*, 96, S56–S72. <https://doi.org/10.1785/0120050822>
- Kammer, D. S., Radiguet, M., Ampuero, J.-P., & Molinari, J.-F. (2015). Linear elastic fracture mechanics predicts the propagation distance of frictional slip. *Tribology Letters*, 57(3), 1–10. <https://doi.org/10.1007/s11249-014-0451-8>
- Kaneko, Y., & Ampuero, J.-P. (2011). A mechanism for preseismic steady rupture fronts observed in laboratory experiments. *Geophysical Research Letters*, 38, L21307. <https://doi.org/10.1029/2011GL049953>
- Kaneko, Y., & Lapusta, N. (2008). Variability of earthquake nucleation in continuum models of rate-and-state faults and implications for aftershock rates. *Journal of Geophysical Research*, 113, B12312. <https://doi.org/10.1029/2007JB005154>
- Kaneko, Y., Nielsen, S. B., & Carpenter, B. M. (2016). The onset of laboratory earthquakes explained by nucleating rupture on a rate-and-state fault. *J. Geophys. Res. Solid Earth*, 121. <https://doi.org/10.1002/2016JB013143>
- Kato, A., Obara, K., Igarashi, T., Tsuruoka, H., Nakagawa, S., & Hirata, N. (2012). Propagation of slow slip leading up to the 2011 Mw 9.0, Tohoku-Oki earthquake. *Science*, 335(6069), 705–708. <https://doi.org/10.1126/science.1215141>
- Kato, N., Yamamoto, H., & Hirasawa, T. (1992). Strain-rate effect on frictional strength and the slip nucleation process. *Tectonophysics*, 211(1), 269–282. [https://doi.org/10.1016/0040-1951\(92\)90064-d](https://doi.org/10.1016/0040-1951(92)90064-d)
- Ke, C. Y., McLaskey, G. C., & Kammer, D. S. (2018). Rupture termination in laboratory-generated earthquakes. *Geophysical Research Letters*, 45(23), 12–784. <https://doi.org/10.1029/2018GL080492>
- Kwiatek, G., Plenkens, K., Nakatani, M., Yabe, Y., Dresen, G., & JAGUARS-Group (2010). Bulletin of the. *Seismological Society of America*, 100(3), 1165–1173. <https://doi.org/10.1785/0120090277>
- Lapusta, N., & Rice, J. R. (2003). Nucleation and early seismic propagation of small and large events in a crustal earthquake model. *Journal of Geophysical Research*, 108(B4), 2205. <https://doi.org/10.1029/2001JB000793>
- Latour, S., Schubnel, A., Nielsen, S., Madariaga, R., & Vinciguerra, S. (2013). Characterization of nucleation during laboratory earthquakes. *Geophysical Research Letters*, 40, 5064–5069. <https://doi.org/10.1002/grl.50974>
- Liao, Z., Chang, J., & Reches, Z. (2014). Fault strength evolution during high velocity friction experiments with slip-pulse and constant-velocity loading. *Earth and Planetary Science Letters*, 406, 93–101. <https://doi.org/10.1016/j.epsl.2014.09.010>
- Linde, A. T., Gladwin, M. T., Johnston, M. J., Gwyther, R. L., & Bilham, R. G. (1996). A slow earthquake sequence on the San Andreas fault. *Nature*, 383(6595), 65. <https://doi.org/10.1038/383065a0>
- Liu, Y., & Rice, J. R. (2005). Aseismic slip transients emerge spontaneously in three-dimensional rate and state modeling of subduction earthquake sequences. *Journal of Geophysical Research*, 110, B08307. <https://doi.org/10.1029/2004JB003424>
- Luo, Y., & Ampuero, J.-P. (2018). Stability of faults with heterogeneous friction properties and effective normal stress. *Tectonophysics*, 733(2018), 257–272. <https://doi.org/10.1016/j.tecto.2017.11.006>
- Marone, C., & Kilgore, B. (1993). Scaling of the critical slip distance for seismic faulting with shear strain in fault zones. *Nature*, 362, 618–621. <https://doi.org/10.1038/362618a0>
- McGuire, J. J., Collins, J. A., Gouédard, P., Roland, E., Lizaralde, D., Boettcher, M. S., et al. (2012). Variations in earthquake rupture properties along the Gofar transform fault, East Pacific Rise. *Nature Geoscience*, 5(5), 336–341. <https://doi.org/10.1038/ngeo1454>
- McLaskey, G. C., & Kilgore, B. D. (2013). Foreshocks during the nucleation of stick-slip instability. *Journal of Geophysical Research: Solid Earth*, 118, 2982–2997. <https://doi.org/10.1002/jgrb.50232>
- McLaskey, G. C., Kilgore, B. D., & Beeler, N. M. (2015). Slip-pulse rupture behavior on a 2 meter granite fault. *Geophysical Research Letters*, 42, 12–784. <https://doi.org/10.1002/2015GL065207>
- McLaskey, G. C., & Lockner, D. A. (2014). Preslip and cascade processes initiating laboratory stick-slip. *Journal of Geophysical Research: Solid Earth*, 119, 6323–6336. <https://doi.org/10.1002/2014JB011220>
- McLaskey, G. C., & Lockner, D. A. (2018). Shear failure of a granite pin traversing a sawcut fault. *International Journal of Rock Mechanics and Mining Sciences*, 110, 97–110. <https://doi.org/10.1016/j.ijrmms.2018.07.001>
- McLaskey, G. C., & Yamashita, F. (2017). Slow and fast ruptures on a laboratory fault controlled by loading characteristics. *Journal of Geophysical Research: Solid Earth*, 122, 3719–3738. <https://doi.org/10.1002/2016JB013681>
- Nadeau, R. M., & Johnson, L. R. (1998). Seismological studies at Parkfield VI: Moment release rates and estimates of source parameters for small repeating earthquakes. *Bulletin of the Seismological Society of America*, 88, 790–814.
- Nielsen, S., Taddeucci, J., & Vinciguerra, S. (2010). Experimental observation of stick-slip instability fronts. *Geophysical Journal International*, 180(2), 697–702. <https://doi.org/10.1111/j.1365-246x.2009.04444.x>
- Noda, H., Nakatani, M., & Hori, T. (2013). Large nucleation before large earthquakes is sometimes skipped due to cascade-up—Implications from a rate and state simulation of faults with hierarchical asperities. *Journal of Geophysical Research: Solid Earth*, 118, 2924–2952. <https://doi.org/10.1002/jgrb.50211>
- Ohnaka, M. (2000). A physical scaling relation between the size of an earthquake and its nucleation zone size. *Pure and Applied Geophysics*, 157(11–12), 2259–2282. <https://doi.org/10.1007/pl00001084>
- Ohnaka, M., & Kuwahara, Y. (1990). Characteristic features of local breakdown near a crack-tip in the transition zone from nucleation to unstable rupture during stick-slip shear failure. *Tectonophysics*, 175, 197–220. [https://doi.org/10.1016/0040-1951\(90\)90138-x](https://doi.org/10.1016/0040-1951(90)90138-x)
- Ohnaka, M., & Shen, L. F. (1999). Scaling of the shear rupture process from nucleation to dynamic propagation: Implications of geometric irregularity of the rupturing surfaces. *Journal of Geophysical Research*, 104, 817–844. <https://doi.org/10.1029/1998jb900007>
- Okubo, P. G., & Dieterich, J. H. (1984). Effects of physical fault properties on frictional instabilities produced on simulated faults. *Journal of Geophysical Research*, 89(B7), 5817–5827. <https://doi.org/10.1029/jb089ib07p05817>
- Okuda, S., & Ide, S. (2018). Hierarchical rupture growth evidenced by the initial seismic waveforms. *Nature Communications*, 9, 3714. <https://doi.org/10.1038/s41467-018-06168-3>
- Ozawa, S. W., Hatano, T., & Kame, N. (2019). Longer migration and spontaneous decay of aseismic slip pulse caused by fault roughness. *Geophysical Research Letters*, 46. <https://doi.org/10.1029/2018GL081465>
- Passelègue, F. X., Schubnel, A., Nielsen, S., Bhat, H. S., & Madariaga, R. (2013). From sub-Rayleigh to supershear ruptures during stick-slip experiments on crustal rocks. *Science*, 340, 1208–1211. <https://doi.org/10.1126/science.1235637>
- Ray, S., & Viesca, R. C. (2017). Earthquake nucleation on faults with heterogeneous frictional properties, normal stress. *Journal of Geophysical Research: Solid Earth*, 122, 8214–8240. <https://doi.org/10.1002/2017JB014521>

- Rice, J. R. (1993). Spatio-temporal complexity of slip on a fault. *Journal of Geophysical Research*, 98(B6), 9885–9907.
- Roeloffs, E. A. (2006). Evidence for aseismic deformation rate changes prior to earthquakes. *Annual Review of Earth and Planetary Sciences*, 34, 591–627. <https://doi.org/10.1146/annurev.earth.34.031405.124947>
- Rosakis, A., Kanamori, H., & Xia, K. (2006). Laboratory earthquakes. *International Journal of Fracture*, 138, 211–218. <https://doi.org/10.1007/s10704-006-0030-6>
- Rubin, A. M., & Ampuero, J.-P. (2005). Earthquake nucleation on (aging) rate and state faults. *Journal of Geophysical Research*, 110, B11312. <https://doi.org/10.1029/2005JB003686>
- Rubin, A. M., & Ampuero, J.-P. (2009). Self-similar slip pulses during rate-and-state earthquake nucleation. *Journal of Geophysical Research, Solid Earth*, 114(B11). <https://doi.org/10.1029/2009jb006529>
- Rubin, A. M., Gillard, D., & Got, J. L. (1999). Streaks of microearthquakes along creeping faults. *Nature*, 400(6745), 635–641. <https://doi.org/10.1038/23196>
- Rubinstein, S. M., Cohen, G., & Fineberg, J. (2004). Detachment fronts and the onset of dynamic friction. *Nature*, 430, 1005–1009. <https://doi.org/10.1038/nature02830>
- Ruiz, S., Aden-Antoniow, F., Baez, J. C., Otarola, C., Potin, B., del Campo, F., & Bernard, P. (2017). Nucleation phase and dynamic inversion of the Mw 6.9 Valparaíso 2017 earthquake in Central Chile. *Geophysical Research Letters*, 44(10), 290–10,297. <https://doi.org/10.1002/2017GL075675>
- Saffer, D. M., & Wallace, L. M. (2015). The frictional, hydrologic, metamorphic and thermal habitat of shallow slow earthquakes. *Nature Geoscience*, 8, 594–600. <https://doi.org/10.1038/ngeo2490>
- Savage, H. M., Keranen, K. M., Schaff, D. P., & Dieck, C. (2017). Possible precursory signals in damage zone foreshocks. *Geophysical Research Letters*, 44, 5411–5417. <https://doi.org/10.1002/2017GL073226>
- Schaal, N., & Lapusta, N. (2019). Microseismicity on patches of higher compression during larger-scale earthquake nucleation in a rate-and-state fault model. *Journal of Geophysical Research: Solid Earth*, 124, 1962–1990. <https://doi.org/10.1029/2018JB016395>
- Scholz, C. H. (2002). *The mechanics of earthquakes and faulting*. s.l. Cambridge University Press.
- Scuderi, M., Collettini, C., Viti, C., Tinti, E., & Marone, C. (2017). Evolution of shear fabric in granular fault gouge from stable sliding to stick slip and implications for fault slip mode. *Geology*, 45(8), 731–734. <https://doi.org/10.1130/g39033.1>
- Skarbek, R., Rempel, A., & Schmidt, D. (2012). Geologic heterogeneity can produce aseismic slip transients. *Geophysical Research Letters*, 39(21), L21306. <https://doi.org/10.1029/2012GL053762>
- Tal, Y., Hager, B. H., & Ampuero, J. P. (2018). The effects of fault roughness on the earthquake nucleation process. *Journal of Geophysical Research: Solid Earth*, 123(1), 437–456. <https://doi.org/10.1002/2017jb014746>
- Tape, C., Holtkamp, S., Silwal, V., Hawthorne, J., Kaneko, Y., Ampuero, J. P., et al. (2018). Earthquake nucleation and fault slip complexity in the lower crust of Central Alaska. *Nature Geoscience*, 11, 536–541. <https://doi.org/10.1038/s41561-018-0144-2>
- Tape, C., West, M., Silwal, V., & Ruppert, N. (2013). Earthquake nucleation and triggering on an optimally oriented fault. *Earth and Planetary Science Letters*, 363, 231–241. <https://doi.org/10.1016/j.epsl.2012.11.060>
- Thompson, B. D., Young, R. P., & Lockner, D. A. (2009). Premonitory acoustic emissions and stick-slip in natural and smooth-faulted Westerly granite. *Journal of Geophysical Research*, 114, B02205. <https://doi.org/10.1029/2008JB005753>
- Tse, S. T., & Rice, J. R. (1986). Crustal earthquake instability in relation to the depth variation of frictional slip properties. *Journal of Geophysical Research*, 91, 9452–9472. <https://doi.org/10.1029/jb091ib09p09452>
- Uchida, N., Matsuzawa, T., Ellsworth, W. L., Imanishi, K., Shimamura, K., & Hasegawa, A. (2012). Source parameters of microearthquakes on an interplate asperity off Kamaishi, NE Japan over two earthquake cycles. *Geophysical Journal International*, 189, 999–1014. <https://doi.org/10.1111/j.1365-246X.2012.05377.x>
- Uchide, T., & Ide, S. (2010). Scaling of earthquake rupture growth in the Parkfield area: Self-similar growth and suppression by the finite seismogenic layer. *Journal of Geophysical Research*, 115, B11302. <https://doi.org/10.1029/2009JB007122>
- Uenishi, K., & Rice, J. R. (2003). Universal nucleation length for slip-weakening rupture instability under nonuniform fault loading. *Journal of Geophysical Research*, 108(B1), 2042. <https://doi.org/10.1029/2001JB001681>
- Vidale, J. E., Ellsworth, W. L., Cole, A., & Marone, C. (1994). Variations in rupture process with recurrence interval in a repeated small earthquake. *Nature*, 368, 624–626. <https://doi.org/10.1038/368624a0>
- Viesca, R. C. (2016). Stable and unstable development of an interfacial sliding instability. *Physical Review E*, 93, 060202. <https://doi.org/10.1103/physreve.93.060202>
- Wu, B. S., & McLaskey, G. C. (2019). Contained laboratory earthquakes ranging from slow to fast. *Journal of Geophysical Research: Solid Earth*. <https://doi.org/10.1029/2019JB017865>
- Xu, S., Fukuyama, E., & Yamashita, F. (2019). *Robust estimation of rupture properties at propagating front of laboratory earthquakes*, (p. 124). *Journal of Geophysical Research: Solid Earth*. <https://doi.org/10.1029/2018JB016797>
- Xu, S., Fukuyama, E., Yamashita, F., Mizoguchi, K., Takizawa, S., & Kawakata, H. (2018). Strain rate effect on fault slip and rupture evolution: Insight from meter-scale rock friction experiments. *Tectonophysics*, 733, 209–231. <https://doi.org/10.1016/j.tecto.2017.11039>
- Yamashita, F., Fukuyama, E., Xu, S., Mizoguchi, K., Kawakata, H., & Takizawa, S. (2018). Rupture preparation process controlled by surface roughness on meter-scale laboratory fault. *Tectonophysics*, 733, 193–208. <https://doi.org/10.1016/j.tecto.2018.01.034>
- Zhuo, Y.-Q., Liu, P., Chen, S., Guo, Y., & Ma, J. (2018). Laboratory observations of tremor-like events generated during preslip. *Geophysical Research Letters*, 45. <https://doi.org/10.1029/2018GL079201>